

1 **Convective transition statistics over tropical oceans for climate model**
2 **diagnostics: Observational baseline**

3
4 Yi-Hung Kuo, * Kathleen A. Schiro, and J. David Neelin

5 *Department of Atmospheric and Oceanic Sciences, University of California Los*
6 *Angeles, Los Angeles, CA, USA*

7
8 Corresponding Author:

9 Yi-Hung Kuo

10 Dept. of Atmospheric and Oceanic Sciences, University of California, Los Angeles

11 405 Hilgard Ave., Los Angeles, CA 90095-1565

12 Email: yhkuo@atmos.ucla.edu

13

Abstract

14 Convective transition statistics, which describe the relation between column-integrated water
15 vapor (CWV) and precipitation, are compiled over tropical oceans using satellite and ARM site
16 measurements to quantify the temperature and resolution dependence of the precipitation-
17 CWV relation at fast timescales relevant to convection. At these timescales, and for
18 precipitation especially, uncertainties associated with observational systems must be addressed
19 by examining features with a variety of instrumentation, and identifying robust behaviors
20 versus instrument sensitivity at high rain rates. Here the sharp pickup in precipitation as CWV
21 exceeds a certain critical threshold is found to be insensitive to spatial resolution, with
22 convective onset occurring at higher CWV but at lower column relative humidity as bulk
23 tropospheric temperature increases. Mean tropospheric temperature profiles conditioned on
24 precipitation show vertically coherent structure across a wide range of temperature,
25 reaffirming the use of a bulk temperature measure in defining the convective transition
26 statistics. The joint probability distribution of CWV and precipitation develops a peak
27 probability at low precipitation for CWV above critical, with rapid decreasing probability of high
28 precipitation below and near critical, and exhibits systematic changes under spatial-averaging.
29 The precipitation pickup with CWV is reasonably insensitive to time-averaging up to several
30 hours but is smoothed at daily timescales. This work demonstrates that CWV relative to critical
31 serves as an effective predictor of precipitation with only minor geographic variations in the
32 tropics, quantifies precipitation-related statistics subject to different spatial-temporal
33 resolution, and provides a baseline for model comparison to apply these statistics as
34 observational constraints on precipitation processes.

35 **1. Introduction**

36 Despite the ongoing improvement of weather and climate modeling in recent decades in
37 terms of model resolution and number of simulated processes, convective parameterization
38 remains a major contributor to the uncertainty of future projection (Sanderson 2011; Rowell
39 2012; Yokohata et al. 2012; Sherwood et al. 2014) and systematic biases in precipitation and
40 clouds persist. A non-exhaustive list of persistent biases includes the double-ITCZ bias (Mapes
41 and Neale 2011; Hirota et al. 2014), insensitivity of precipitation to environment humidity
42 (Oueslati and Bellon 2013), low bias in tropospheric humidity (Gonzalez and Jiang 2017), failing
43 to capture the amplitude and propagation of MJO (Kim et al. 2014; Jiang et al. 2016, 2017),
44 unrealistic statistics and surface storm tracks for tropical cyclones (Booth et al. 2017), and
45 incorrect precipitation diurnal cycle over land (Covey et al. 2016). These biases also impact
46 model diagnosis for short-term forecasting purposes, since models adopted for weather
47 forecasting or reanalysis share common components with climate models.

48 Many conventional diagnostics for climate models emphasize comparisons against long-term
49 climatology or variability at different timescales, and the model performance examined by
50 these metrics are affected by multiple factors. While sensitivity experiments with respect to
51 such metrics are useful in identifying important processes (Benedict et al. 2013, 2014; Boyle et
52 al. 2015; Bernstein and Neelin 2016; Langenbrunner and Neelin 2017), the contribution of
53 certain processes can be difficult to isolate, making constraining model performance
54 challenging. As such, there is an emerging need for diagnostics targeting processes and focusing
55 on the most relevant timescales. This study presents an example of such process-oriented
56 diagnostics – the convective transition statistics – which focus on the fast-timescale deep
57 convection in the tropics.

58 The sensitivity of moist convection to lower free-tropospheric humidity had been suggested
59 by the analysis of TOGA COARE and operational sounding data for the tropical western Pacific
60 (Brown and Zhang 1997; Sherwood and Wahrlich 1999; Parsons et al. 2000), and was
61 subsequently affirmed by numerical experiments (Tompkins 2001; Redelsperger et al. 2002;
62 Ridout 2002; Derbyshire et al. 2004). Later observational and modeling studies pointed to the
63 importance of organized convective systems in determining the environment moisture field
64 (Tao and Moncrieff 2009; Yano et al. 2012; Moncrieff et al. 2017). Bretherton et al. (2004)
65 documented an empirical relationship between the column relative humidity (CRH) and
66 precipitation over tropical oceans at daily and monthly timescales in SSM/I satellite retrievals
67 (see also Rushley et al. 2018). Based on the analysis of the same satellite observations at fast
68 timescales, Peters and Neelin (2006) noted a sharp increase in precipitation as the column-
69 integrated water vapor (CWV) exceeded a certain threshold, and, using the analogy to
70 associated behavior in continuous phase transitions, showed consistent relations among a set

71 of statistics including probability and variance of precipitation, and the distribution of CWV for
72 precipitating events. Subsequent studies have examined the dependence on tropospheric
73 temperature (Neelin et al. 2009) and how the statistics can be reproduced by simple stochastic
74 models (Stechmann and Neelin 2011, 2014). The plume buoyancy calculations based on
75 ground-based measurements at tropical ARM sites (Holloway and Neelin 2009; Schiro et al.
76 2016) and the NCAR CAM5 simulations (Sahany et al. 2012; Kuo et al. 2017) have demonstrated
77 that entrainment is instrumental in explaining the observed precipitation-CWV relation, and
78 that the relation is qualitatively robust over land and ocean. These convective transition
79 statistics characterize the dependence of tropical convection on bulk measures of the water
80 vapor-temperature environment.

81 The robust rapid increase in conditionally-averaged precipitation and conditional probability
82 of precipitation as CWV exceeds a certain threshold (the “pickup of precipitation”) derived from
83 the tropical ARM sites have been used to constrain the entrainment parameter in the NCAR
84 CESM (Kuo et al. 2017). Given that precipitation-related statistics are sensitive to resolution
85 (Chen and Dai 2017; Klingaman et al. 2017), to allow for a more quantitative comparison to
86 model output subject to varying spatial resolution and temporal frequency, the dependence of
87 the convective transition statistics on spatial-temporal resolution must be quantified. Moreover,
88 the robustness to instrumentation, especially at high rain rate, should be addressed to ensure
89 the reliability of such diagnostics. The purposes of this study are to quantify the resolution
90 dependence and robustness of the statistics, provide an observational baseline for model
91 comparison, and to expand the set of related properties that can be understood within this
92 framework.

93 This manuscript is organized as follows. Section 2 describes the datasets analyzed here. The
94 basic convective transition statistics, which build on those introduced in previous work (e.g.,
95 Peters and Neelin 2006; Neelin et al. 2008), are presented in Section 3 with the following
96 additions: using newer datasets, assessing the spatial-resolution dependence of the statistics,
97 testing the robustness to instrumentation and evaluating sensitivity to the choice of bulk
98 measure of tropospheric temperature. Sections 4-6 explore new statistics characterizing the
99 convective transition. Section 4 examines the geographic variations, or the lack thereof, of the
100 effectiveness of CWV relative to critical as a predictor of precipitation, and the associated
101 dependences on spatial-temporal resolution. The sensitivity of the statistics to time-averaging is
102 discussed in Section 5. The joint-PDF of CWV and precipitation, and its dependence on spatial
103 resolution and instrumentation, are shown in Section 6. Finally, Section 7 summarizes the
104 properties of convective transition statistics, and briefly discusses their potential as diagnostic
105 tools.

106

107 **2. Datasets**

108 Compiling the convective transition statistics requires column-integrated water vapor CWV,
109 precipitation rate P , column-integrated saturation humidity $\widehat{q}_{sat} [\equiv \int q_{sat}(T(p), p) dp/g$; here
110 $q_{sat}(T(p), p)$ is the saturation specific humidity with respect to liquid water as a function of
111 temperature $T(p)$ and pressure p], and mass-weighted column-averaged temperature \widehat{T} .

112 The primary source of CWV and P here is the TRMM Microwave Imager (TMI) retrieval
113 products processed by Remote Sensing Systems (RSS; algorithm v7.1; TMIv7.1 hereafter; Wentz
114 et al. 2015). The retrieved values include gridded ($0.25^\circ \times 0.25^\circ$) snapshots of CWV (units: 0.3
115 mm) and P (units: 0.1 mm hr^{-1}) over ocean, with no data available over land. The TRMM
116 Precipitation Radar (PR) 2A25 (v7; available at
117 https://disc.gsfc.nasa.gov/datacollection/TRMM_2A25_7.html) and TRMM 3B42 (v7;
118 https://disc.gsfc.nasa.gov/datacollection/TRMM_3B42_7.html) Rainfall Rate products are used
119 for comparison. The 2A25 data provides snapshots of P with resolution $\sim 5 \text{ km} \times 5 \text{ km}$, and
120 3B42 provides gridded ($0.25^\circ \times 0.25^\circ$) P every 3 hours. Note that 3B42 is a merged product; as
121 such, most values should be interpreted as instantaneous, since P is observed during a specific
122 3-hour window rather than a computed 3-hourly mean. Here, the TMIv7.1, 2A25, and 3B42
123 data for 01 Jun 2002 – 31 May 2014 are used.

124 The Microwave Radiometer (MWR) CWV and rain gauge P measurements collected from the
125 DOE ARM sites at Nauru ($0^\circ 31' \text{ S}$, $166^\circ 54' \text{ E}$) for 1999-2008 and at Manus ($2^\circ 3' \text{ S}$, $147^\circ 25' \text{ E}$)
126 for 1998-2010 in the tropical western Pacific (both with optical rain gauge), and at the ARM
127 Mobile Facility near Manaus ($3^\circ 7' \text{ S}$, $60^\circ 1' \text{ W}$) for 10 Jan 2014 – 20 Oct 2015 during the
128 GOAmazon campaign (with acoustic rain gauge) are also used to study the sensitivity of the
129 statistics to instrumentation and time-averaging.

130 For column-integrated/averaged \widehat{q}_{sat} and \widehat{T} , with the column being defined as 1000-200 hPa,
131 the 6-hourly 2.5° NCEP-DOE Reanalysis-2 (Kanamitsu et al. 2002) temperature is adopted with
132 necessary interpolation. Since the spatial and temporal autocorrelation scales of temperature
133 are expected to be large in the tropics, the interpolation is justified. To avoid potentially
134 erroneous temperature values from spatial interpolation (e.g., around the Andes and New
135 Guinea), data in the 2.5° -neighborhood of land pixels are excluded for some of the presented
136 statistics.

137 Note that the CWV datasets often do not record a CWV value in the presence of
138 precipitation, and thus gap-filling is required to re-construct missing data [Section S1 in the
139 Supplementary Materials (SM)]. For algorithm choices used for the TMIv7.1 data, the
140 probability of missing CWV depends primarily on P , with the probability increasing from 0 to 1
141 almost linearly as P increases from 2 to 9 mm hr^{-1} . This even affects the tropical mean

142 precipitation, e.g., the annual mean precipitation over tropical oceans (20°S-20°N) is reduced
143 from 3.1 to 2.1 mm day⁻¹ by excluding precipitation without valid CWV retrievals. Therefore, it
144 is necessary to gap-fill these missing CWV values; otherwise, the information comprising the
145 desired statistics would be systematically distorted. Here the default is to simply fill the missing
146 values using the available CWV value at the geographically nearest pixel. The sensitivity of the
147 presented statistics to the gap-filling are included in Section S4 (Figs. S7-S11). Similarly, the raw
148 CWV time series from the tropical ARM site MWR measurements are recorded every 20 s, but
149 exhibit gaps because of the "wet-window" effect. Gaps shorter than 6 hours are filled using
150 linear interpolation as described in Schiro et al. (2016). The gap-filled time series are then used
151 to calculate the mean time series at lower temporal frequencies (e.g., 5-min- or hourly-average).
152 Precipitation observations are available in the CWV gaps and do not have to be interpolated.

153 Additionally, satellite CWV retrievals processed by RSS (including TMIv7.1) have a 75-mm cap
154 set by the algorithm. While CWV rarely exceeds 75 mm, operational soundings occasionally
155 record such events, e.g., weather stations in Ishigakijima (24° 20' N, 124° 10' E; station number
156 47918) and Taipei (25° 02' N, 121° 31' E; 58968) recorded 80.03 and 82.54 mm at 00Z and 12Z,
157 respectively, on 21 Aug 2013 under the influence of Typhoon Trami (data from University of
158 Wyoming Atmospheric Soundings). This serves as a reminder of the imperfect observational
159 systems, and one must keep in mind the uncertainties when applying the presented statistics
160 for model diagnosis.

161

162 **3. Dependence of precipitation-CWV relation on tropospheric temperature and spatial** 163 **resolution**

164 **3.1. Basic features of convective transition statistics**

165 Figure 1 shows the basic convective transition statistics, including the precipitation rate (Fig.
166 1a), probability of precipitation (Fig. 1b; $P > 1.05 \text{ mm hr}^{-1}$), probability density functions (PDFs)
167 of all events (Fig. 1c) and precipitating events (Fig. 1d) conditioned on CWV and \widehat{q}_{sat} for the
168 tropical western Pacific, along with results for other tropical ocean basins (Figs. 1e-1p). Here
169 the statistics are compiled at 0.25° (colored markers) and 0.5° (dots), using \widehat{q}_{sat} as the bulk
170 tropospheric temperature. The standard errors associated with the conditionally averaged
171 precipitation (conditional precipitation hereafter) at 0.25° are smaller than the marker size,
172 because of the large number of counts in each bin (on the order of 10³-10⁵), and thus are
173 omitted. To exclude light precipitation and focus on deep-convective events, a threshold of 1.05
174 mm hr⁻¹ defining precipitating events is chosen, with a natural offset 0.05 since the TMIv7.1
175 precipitation is discretized by 0.1-mm hr⁻¹ units. Note that the PDFs of all events (e.g., Fig. 1c) –
176 i.e., PDFs of CWV – are calculated from the joint-PDF of CWV and \widehat{q}_{sat} , normalized for each

177 basin, by treating CWV as a continuous variable and \widehat{q}_{sat} discretely. These PDFs, when
178 multiplied by the corresponding conditional probabilities (Fig. 1b), give the PDFs for
179 precipitating events (Fig. 1d). The jumps at 75 mm for the PDFs result from the CWV cap set by
180 the retrieval algorithm. For sensitivity to gap-filling, see Section S4 (Figs. S7-S11).

181 For each \widehat{q}_{sat} , the conditional precipitation and probability (Fig. 1; 1st and 2nd col.) pick up
182 sharply as CWV exceeds a certain threshold, referred to as the “critical CWV,” or w_c (defined in
183 Section 3.2), around which the PDF of precipitating events (4th col.) peaks. The precipitation
184 pickup occurs at higher CWV for higher \widehat{q}_{sat} , i.e., w_c is increasing with \widehat{q}_{sat} . The conditional
185 probability would decrease with an increase in the threshold defining precipitating events; i.e.,
186 the probability curves would move towards higher CWV. The spacing between pickup curves
187 (for conditional precipitation and probability) suggests that the behavior for \widehat{q}_{sat} bins ≥ 61 mm
188 ($> 85\%$ of total occurrence over tropical oceans) is slightly different from that in lower \widehat{q}_{sat} bins.
189 Inspection of the geographical distribution of \widehat{q}_{sat} occurrence suggests that low- \widehat{q}_{sat} events are
190 due mostly to systems originating from the extratropics (Section S6).

191 The observed sharp increase in precipitation as CWV exceeds critical has been explained by
192 entraining plume calculations, through which the deep-convective conditional instability can be
193 estimated. As previously demonstrated (Holloway and Neelin 2009; Schiro et al. 2016; Kuo et al.
194 2017), CWV serves as a measure of the impact of environment moisture on plume buoyancy,
195 and hence the instability, through the effects of mixing, as indicated by the precipitation pickup.
196 The dependence of w_c on \widehat{q}_{sat} can be explained through a similar approach (Sahany et al. 2012).

197 In Figure 1, the dots (0.5°) match the colored markers (0.25°) in the 1st and 3rd col.; i.e., the
198 conditional precipitation and PDF of CWV are insensitive to spatial resolution, with small but
199 noticeable decreases in the PDF at highest CWV (above critical). This insensitivity is consistent
200 with the assertion that the autocorrelation spatial scales of CWV and tropospheric temperature
201 are much greater than that of precipitation. Nonetheless, to what extent this holds depends on
202 the gap-filling (Figs. S9-S11 in Section S4). It is also consistent with Yano et al. (2012) which used
203 a cloud-resolving model (CRM) and demonstrated that the conditional precipitation as a
204 function of CWV is quantitatively robust to spatial resolution (up to $\sim 1^\circ$).

205 The conditional probability defined by a fixed nonzero threshold (1.05 mm hr^{-1} ; Fig. 1; 2nd
206 col.) slightly shifts toward lower CWV with spatial coarse-graining, consistent with the greater
207 chances of observing precipitation over a larger area. However, with a much higher threshold
208 (e.g., 15 mm hr^{-1} , the practical maximum for TMIv7.1 precipitation in the tropics) or at even
209 lower resolution (e.g., 2°), the dependence on spatial resolution may reverse for the rarer
210 chances of seeing extreme rainfall over a larger area. These dependences indicate the
211 underlying joint-PDF of CWV and P being resolution-sensitive, as will be discussed in Section 6.

212

213 3.2. Critical CWV w_c and collapsed statistics

214 As described earlier, CWV measures the impact of environment moisture on conditional
215 instability, and hence precipitation. For those \widehat{q}_{sat} bins most relevant in the tropics (≥ 61 mm),
216 the pickup curves in Fig. 1 suggest the possibility of collapsing statistics by shifting CWV by w_c
217 for each \widehat{q}_{sat} , i.e., the precipitation-CWV relation can be simplified by taking into account the
218 dependence of w_c on temperature. To define w_c as a function of \widehat{q}_{sat} , it makes sense to do so
219 based on conditional precipitation alone, for it, unlike the conditional probability, does not rely
220 on any threshold and is insensitive to spatial resolution. This assumes that the conditional
221 precipitation has the form of $f(cwv - w_c)$, with its \widehat{q}_{sat} -dependence implicitly built in through
222 $w_c(\widehat{q}_{sat})$. See Section S3 regarding details on finding w_c given the statistics as in Fig. 1.

223 Figures 2a-2d show the collapsed version of the original statistics for the tropical western
224 Pacific in Fig. 1a-1d (other basins in Fig. S6). As in Fig. 2a, w_c is defined as the CWV value at
225 which the best-fit for conditional precipitation (gray line) intersects with the CWV axis. For \widehat{q}_{sat}
226 bins ≥ 70 mm, the conditional precipitation, probability of precipitation (Fig. 2b), and PDF of
227 precipitating events (Fig. 2d) collapse perfectly. For these \widehat{q}_{sat} bins, there are below-critical
228 precipitating events, many of which are weakly precipitating and excluded because of the 1.05-
229 mm hr⁻¹ threshold adopted here, and are likely associated with the mature and decaying phases
230 of convection (not shown). As \widehat{q}_{sat} increases, $\widehat{q}_{sat} - w_c$ (triangles) increases, indicating critical
231 deviates from column saturation. For lower $\widehat{q}_{sat} \leq 61$ mm, both conditional precipitation and
232 probability have slightly higher (lower) values for CWV right below (above) critical, with some
233 underpopulated CWV bins (open circles) exceeding the corresponding column saturation
234 (triangles), indicating minor inconsistency between the retrieval and reanalysis datasets.
235 Furthermore, there is more below-critical precipitation as \widehat{q}_{sat} decreases (Fig. 2d; even more
236 when a smaller precipitation threshold is adopted), consistent with cold events originating from
237 the extratropics and exhibiting characteristics different from deep convection in the tropics.

238 The PDF of CWV in Fig. 2c also collapses around and above critical, with the PDF of non-
239 precipitating events (including those with $P < 1.05$ mm hr⁻¹) varying with \widehat{q}_{sat} and basin. For
240 CWV slightly lower than critical, the PDF of CWV starts to drop rapidly, and the PDF for
241 precipitating events peaks. As demonstrated in simple stochastic models (Stechmann and
242 Neelin 2011, 2014), moisture accumulates by surface evaporation and moisture convergence
243 until CWV reaches critical, at which point precipitation becomes an effective sink, leading to the
244 drop in the PDF for CWV above critical. Note that the PDF for all events has another peak at
245 lower CWV because of the balance between surface evaporation and moisture divergence.

246 Earlier studies (Neelin et al. 2009; Sahany et al. 2014) have suggested scaling instead of
 247 shifting by w_c , i.e., considering the form $f(cwv/w_c)$ instead of the shift $f(cwv - w_c)$, to
 248 collapse the statistics. Both are similar to leading order for small differences in w_c , but to
 249 second order have slightly different effects. Scaling preserves the zero CWV value, which can be
 250 important when examining PDFs across the entire CWV range, while shifting is preferred here
 251 because effects near critical seem to be affected by factors that do not scale with w_c . The two
 252 approaches may lead to different interpretations for warming climate, where some of the
 253 simplest arguments tend to rescale moisture by saturation (see Camargo et al. 2014 for a
 254 discussion surrounding saturation deficit vs relative humidity in projecting future tropical
 255 cyclone genesis frequency).

256

257 3.3. Dependence of critical on temperature

258 The collapsed conditional precipitation and probability of precipitation for the tropical
 259 western Pacific at 0.25° in Figs. 2a-2b are duplicated in Figs. 3a-3b, along with the critical CWV
 260 $w_c(\widehat{q}_{sat})$ (Fig. 3c) and critical column relative humidity (critical CRH) $w_c(\widehat{q}_{sat})/\widehat{q}_{sat}$ (Fig. 3d).
 261 Results for other basins are also shown. Here, we focus on the results derived using TMIv7.1
 262 CWV and precipitation.

263 In Figs. 3a-3d, the precipitation pickup and the dependence of w_c on \widehat{q}_{sat} are constant across
 264 basins, with slightly lower w_c for the tropical Atlantic. As noted earlier, a clear transition occurs
 265 around $\widehat{q}_{sat} = 61$ mm in Figs. 3c-3d. For lower \widehat{q}_{sat} , the precipitation pickup is less well-defined
 266 and scatters more, and so do the corresponding critical values, with approximately constant
 267 critical CRH. Above the transition \widehat{q}_{sat} , the critical values deviate from saturation as \widehat{q}_{sat}
 268 increases, i.e., deep convective onset occurs at higher CWV but at lower CRH with increasing
 269 tropospheric temperature, as shown in Neelin et al. (2009). The critical CRH decreasing with
 270 \widehat{q}_{sat} is expected to be robust as long as w_c is defined through collapsing statistics, for other
 271 reasonable definition of critical [e.g., assuming the functional form of $\log(1 + e^{\alpha(cwv-w_c)})$ for
 272 the conditional precipitation] would only introduce a \widehat{q}_{sat} -independent offset of w_c , preserving
 273 the slope of the w_c - \widehat{q}_{sat} relation which, when compared with the constant CRH (gray) lines in
 274 Fig. 3c, indicates decreasing critical CRH with \widehat{q}_{sat} .

275 The transition from approximately constant to decreasing critical CRH with increasing \widehat{q}_{sat}
 276 marks the different precipitation regimes, i.e., convection-dominant in the tropics vs. large-
 277 scale saturation-driven in the extratropics.

278

279 3.4. Robustness to instrumentation

280 Before the convective transition statistics can be used for model diagnostics, their
281 robustness and sensitivity to instrumentation must be quantified. Figures 3a-3d include the
282 results derived using multiple datasets, including (i) TMIv7.1 CWV and precipitation, (ii) TMIv7.1
283 CWV and PR 2A25 precipitation, and (iii) ground-based measurements from Manus and Nauru
284 ARM sites in the tropical western Pacific.

285 The statistics in Figs. 3a-3d are robust to TMIv7.1 vs. PR precipitation, with slightly more
286 scatter for the conditional probability. Combining TMIv7.1 CWV and 3B42 precipitation results
287 in quantitatively similar statistics except for a slightly smaller slope α of the best-fit for
288 conditional precipitation (not shown).

289 In Fig. 3a, the conditional precipitation from Manus and Nauru ground-based measurements,
290 collapsed using $w_c(\widehat{q}_{sat})$ for the tropical western Pacific (WPac; TMIv7.1 CWV + precipitation),
291 are quantitatively consistent with those from satellite retrievals, with significant low bias at
292 highest CWV (relative to critical; $cwv - w_c > 5$ mm); the corresponding conditional probability
293 in Fig. 3b is uniformly lower than satellite retrievals because of the difference in spatial-
294 resolution, with the similar low bias. Combining the ground-based CWV time series and 3B42
295 precipitation around Manus and Nauru shows the same bias at high CWV, indicating that the
296 cause is due to the ground-based MWR CWV measurements (Section S8). These have a “wet-
297 window” problem, i.e., high CWV events associated with strong precipitation are missing in the
298 raw CWV time series, and gap-filling can only partially compensate for this.

299 Although not the focus here, conditional precipitation and probability at the Manaus
300 GOAmazon site (over land) exhibits quantitative differences from those over oceans as in Fig. 3,
301 despite the qualitative similarities we shall discuss in Section 5.

302 The quantitative agreement among datasets examined here boosts our confidence in the
303 reliability of the convective transition statistics as model diagnostic tools. Meanwhile, given
304 that the same TMIv7.1 CWV and Reanalysis-2 temperature are used for compiling the statistics,
305 we advise caution that the robustness of the statistics to TMIv7.1 vs. PR precipitation may
306 simply reflect the efforts of calibration among datasets. As indicated by the minor difference in
307 the collapsed conditional probabilities in Fig. 3b, and as we shall see in Section 6, the two
308 precipitation datasets do lead to quantitative differences in the distribution of precipitation,
309 especially at high rain rate.

310

311 **3.5. Robustness to bulk measure of temperature**

312 Thus far, \widehat{q}_{sat} appears to be a useful bulk measure of tropospheric temperature. As noted
313 above, the critical value is not governed by \widehat{q}_{sat} in a simple way, with critical CWV increasing
314 and critical CRH decreasing with \widehat{q}_{sat} .

315 Figure 4 shows the temperature profile, conditioned on precipitation and \widehat{q}_{sat} , relative to
316 the mean profile (referred to as a perturbation). The perturbed profile evolves coherently in the
317 vertical as a function of \widehat{q}_{sat} , explaining the usefulness of a bulk temperature measure such as
318 \widehat{q}_{sat} , or the mass-weighted column-averaged temperature \widehat{T} adopted in previous studies (e.g.,
319 Holloway and Neelin 2007; Sahany et al. 2012). The profiles are similar across basins, except for
320 the high- and low- \widehat{q}_{sat} bins in the tropical Indian Ocean showing greater (smaller) anomaly in
321 the lower (upper) troposphere. This is likely a consequence of the circulation pattern driven by
322 the local land-ocean contrast, since both the warmest and coldest events in this domain tend to
323 occur near the south Asian continent in the Bay of Bengal and Arabian Sea (Fig. S13). The
324 resulting statistics in Figs. 1-3, nevertheless, do not reflect this difference in temperature
325 structure. Replacing the condition on precipitation by CWV above critical, or replacing \widehat{q}_{sat} by \widehat{T} ,
326 leads to similar profiles. For \widehat{q}_{sat} higher than the most probable bin, the corresponding overall
327 (perturbed + mean) temperature profiles are insensitive to conditions on precipitation or CWV,
328 suggesting that high- \widehat{q}_{sat} events result from previous or nearby convective activity, consistent
329 with convection being the major heating mechanism in the tropical troposphere.

330 The two bulk measures \widehat{q}_{sat} and \widehat{T} , both of which have similar properties in characterizing
331 convection, are well-correlated because of the vertical coherence of temperature (Section S2).
332 It is nonetheless worth quantifying in detail their similarity as bulk temperature measures for
333 the statistics because of the nonlinear dependence of precipitation statistics on the
334 thermodynamic variables. The lower panels of Figs. 2-3 show the similar statistics
335 corresponding to their upper-panel counterparts, but use \widehat{T} instead as the bulk measure (other
336 basins in Fig. S5). From these two figures, substituting one bulk measure by another only leads
337 to minor quantitative differences, e.g., a slightly smaller slope α for conditional precipitation
338 (Figs. 2a vs 2e), and slightly more precipitating events for CWV right below critical for cold bins
339 when \widehat{q}_{sat} is used (Figs. 2d vs 2h). This insensitivity to the bulk measure of temperature also
340 holds for statistics presented in Figs. 5 and 7-9 below. Note that the vertically coherent
341 temperature structure in the presence of convection guarantees that layered bulk measures
342 (e.g., 850-500 hPa-integrated saturation humidity, etc.) can also be useful and would lead to
343 similar statistics (e.g., Figs. 1 and 3 in Neelin et al. 2009), except for the PDF of all events for
344 CWV significantly lower than critical, which could differ qualitatively (not shown).

345

346 4. Geographical dependence of precipitation pickup

347 The statistics in Figs. 2-3 demonstrate that CWV above critical is a practical estimator of
 348 conditional instability, and hence precipitation, with the temperature dependence
 349 characterized by the w_c -temperature relation [$w_c(\widehat{q}_{sat})$ or $w_c(\widehat{T})$]. These relations seem to be
 350 universal across ocean basins, at basin scales. However, other factors contributing to
 351 conditional instability – vertical degrees of freedom of temperature and moisture structure not
 352 captured by the bulk measures used here, large-scale convergence/divergence, radiative
 353 forcing associated with existing clouds or the lack thereof, and triggering of convection because
 354 of cold pool expansion from organized systems or land-sea breeze in coastal regions – may vary
 355 geographically, causing geographic variations at regional scales (e.g., Torri et al. 2015;
 356 Bergemann and Jakob 2016; Ahmed and Schumacher 2017). As such, the effectiveness of CWV
 357 above critical as a predictor of precipitation at regional scales is examined in this section.

358 As background for our discussion, Fig. 5a shows the probability of precipitation ($P > 0.25$ mm
 359 hr^{-1} ; details in caption). The probability of high CWV (relative to critical; Fig. S14a) is included in
 360 Section S7. These maps of probability of precipitation and high CWV reflect the climatology of
 361 precipitation (Fig. S14b), sharply contrasting the major convergence zones with regions
 362 elsewhere.

363 Figure 5b shows the corresponding conditional probability of precipitation given high CWV,
 364 formally defined as

$$365 \text{Prob}(P > 0.25 \text{ mm hr}^{-1} | cwv > w_c - 1.5 \text{ mm}) \equiv$$

$$366 \frac{\# \text{ of occurrences with } P > 0.25 \text{ mm hr}^{-1} \ \& \ cwv > w_c - 1.5 \text{ mm}}{\# \text{ of occurrences with } cwv > w_c - 1.5 \text{ mm}},$$

367 as a function of geographical location. Here the critical value $w_c(\widehat{q}_{sat})$ is from Fig. 3c, averaged
 368 over four basins (adopting basin-dependent critical values only introduces small discontinuities
 369 in w_c hence the conditional probability across basin boundaries). The most outstanding feature
 370 in Fig. 5b is that the conditional probability is far smoother than the probability of precipitation
 371 in Fig. 5a. To the extent that there are geographic variations, the conditional probability
 372 scarcely reflects the features of precipitation climatology. Thus, including CWV relative to
 373 critical and the dependence of critical on temperature has yielded a probability measure that is
 374 much less dependent on space.

375 To a first approximation, the CWV value relative to critical thus provides information that
 376 will apply reasonably well across a large portion of the Tropics. Furthermore, compiling the
 377 statistics presented in Fig. 3 inside and outside regions with high seasonal precipitation yields
 378 quantitatively similar results (not shown; refer to Fig. 3 since the corresponding collapsed
 379 statistics and critical values are visually indistinguishable), reaffirming that these statistics focus
 380 on the occurrences of convection at fast timescales rather than long-term climatology.

381 Minor geographic variations may be noted in Fig. 5b, e.g., the contrast between the lower
382 values around the Maritime Continent and along the equator in the eastern Pacific, and the
383 higher values off the equator in the central-to-eastern Pacific and Atlantic. The conditional
384 probability is not defined over dry regions covered by marine stratocumulus (there are not
385 above-critical events occurring in these locations); where it is defined, there is large uncertainty
386 associated with small sample size along the edges of the dry regions (e.g., along 10° S in the
387 eastern Pacific). The extreme low values in some coastal regions (~ 2.5° in width, the resolution
388 of Reanalysis-2 data) could be due to physical coastal effects (Bergemann and Jakob 2016).
389 However, local decreases in the temperature (Fig. 3 in Kuo et al. 2017) suggest they are more
390 likely due to the erroneously lower \widehat{q}_{sat} (and hence w_c) and spurious occurrence of above-
391 critical events arising from land-ocean temperature contrasts and spatial interpolation.

392 Figures 5c and 5d further quantify spatial and temporal dependence of this conditional
393 probability. Figure 5c shows the same conditional probability as in Fig. 5b, but at 1°. Coarse-
394 graining in space leads to the same spatial pattern (or the lack thereof) and, with the 0.25-mm
395 hr⁻¹ threshold adopted here, uniformly greater magnitude in conditional probability, consistent
396 with the dependence on resolution shown in Figs. 1-2. That is, CWV above critical serves as a
397 precipitation estimator with more certainty at scales comparable to or larger than the
398 autocorrelation spatial scale of precipitation.

399 Figure 5d shows the conditional probability as in Fig. 5b, but incorporating 3B42
400 precipitation (details in caption). Here, including two additional 3B42 precipitation rate values
401 effectively provides one more independent snapshot of precipitation taken in the period of 0 to
402 4.5 hours prior to or after the TMIv7.1 measurement is acquired. The resulting conditional
403 probability in Fig. 5d therefore quantifies the probability of observing at least one precipitating
404 event from the two datasets, consecutive in time but randomly separated by up to 4.5 hours,
405 given that CWV exceeds critical. Note that here the CWV value relative to critical is treated as
406 approximately constant because of the long autocorrelation timescales of CWV and
407 temperature.

408 As expected, the conditional probability in Fig. 5d (at 0.25°) is everywhere greater than its
409 counterpart in Fig. 5b, and a similar map compiled at 2° is uniformly greater than 85% over
410 tropical oceans (not shown). These suggest that, at scales comparable to the autocorrelation
411 spatial and temporal scales of CWV, an above-critical event is almost certainly accompanied by
412 precipitation before decreasing to below-critical. While precipitation has much shorter
413 autocorrelation timescales, the comparison of Figs. 5b and 5d has ruled out the simplest
414 hypothesis that the two consecutive-in-time measurements of precipitation can be treated as
415 independent random events (not shown).

416 Figure 5e shows the fraction of total precipitation from above-critical events, which are
417 responsible for most of the precipitation over tropical oceans (except in dry regions). It also
418 captures the seasonal shifts of convergence zones, e.g., the local maximum along 10° S in the
419 Indian Ocean and between 0-10° S in the eastern Pacific results from events during the
420 Southern Hemisphere raining seasons.

421 Note that Fig. 5e [and the conditional probability
422 $Prob(cwv > w_c - 1.5 \text{ mm} | P > 0.25 \text{ mm hr}^{-1})$; Fig. S14d] has a geographic pattern similar to
423 Fig. 17 in Tao and Moncrieff (2009; TM09; fraction of precipitation from mesoscale convective
424 systems) with some coastal exceptions. This similarity suggests that organized systems are
425 important contributors to precipitation above critical (see also Moncrieff et al. 2017). As we
426 have seen in Figs. 1-2, the conditional precipitation and PDF of CWV are robust to spatial
427 resolution (up to $\sim 1^\circ$) – in addition to the autocorrelation spatial scale of CWV being greater
428 than that of precipitation, organized systems could play a role in this robustness.

429 Finally, Figure 5f shows an example for ascending orbits on a particular day, showing the
430 regions where CWV is close to or above critical, i.e., a realization of the conditional probability
431 in Fig. 5c for those snapshots on each orbit. Precipitation values exceeding 0.25 mm hr^{-1} are
432 overlaid. It may be seen that precipitation mainly occurs in the near- or above-critical regions
433 sporadically, consistent with the probabilities shown in the earlier panels. Thus, the estimates
434 of near- or above-critical CWV-temperature environment may have useful applications as
435 predictors of precipitation (see also Section S7), making the known association of precipitation
436 with high CWV (e.g., Mapes et al. 2006) more quantitative.

437

438 **5. Sensitivity to time-averaging**

439 Satellite retrievals provide snapshots of CWV and precipitation covering basin-scale areas
440 and, unlike most ground-based data, contain enough events for the compiled statistics to be
441 stable, i.e., insensitive to noise. However, when these statistics apply to model diagnostics –
442 given that most current models output at sub-daily frequencies (e.g., 6- or 12-hourly means)
443 and higher frequency output (e.g., hourly or time-step mean/snapshot) are not standard yet –
444 the validity of the model vs. retrieval comparison must be addressed. To quantify the
445 dependence on coarse-graining in time, we turn to ground-based measurements that have
446 more extensive time-domain information.

447 Figure 6 shows statistics from tropical ARM site measurements with different time-averaging
448 (not conditioned on temperature). At these sites, the temperature range in terms of \hat{T} is
449 narrow, with $\sim 1\text{-}2 \text{ K}$ variation, and hence the overall statistics are dominated by the most
450 probable temperature bin. The conditional precipitation (1st col.) and frequency density for all

451 events (3rd col.; crosses) are relatively insensitive to time-averaging up to 6 hours, with Nauru
452 being more sensitive than the other two sites. Conditional probability (2nd col.; $P > 0.5 \text{ mm hr}^{-1}$)
453 increases with time-averaging, reflecting the sensitivity of the joint-PDF of CWV and
454 precipitation. There are quantitative differences among these sites, but there is not a clear
455 qualitative difference or contrast between oceanic vs. continental environments regarding the
456 dependence on time-averaging. The sharpness of the pickup tends to be smoothed out by the
457 averaging, resulting from averaging sub-daily instances of high CWV, high precipitation times
458 with lower values. Overall, however, the results in Fig. 6 suggest that, while instantaneous or
459 hourly data are desirable for insights into the fast-timescale behavior, statistics from 3- or 6-
460 hourly mean data can be used for model comparisons, extending the applicability of using these
461 statistics as diagnostic tools.

462

463 **6. Joint-PDF of CWV and precipitation, and its resolution/instrument dependence**

464 As mentioned in Section 4, bulk measures like CWV and \widehat{q}_{sat} (or \widehat{T}) can represent large-scale
465 factors that affect conditional instability. However, given the same condition at large scales,
466 one would still expect a distribution of precipitation because there are processes at smaller
467 scales or large-scale factors that are unaccounted for by the bulk measures. In this section, we
468 examine the joint-PDF of CWV and precipitation, and its dependence on spatial resolution and
469 instrumentation, to quantify the uncertainty associated with the use of the bulk measures. This
470 joint-PDF can be another useful metric for model diagnostics.

471 Figure 7a shows the joint-PDF of CWV (relative to critical) and precipitation rate P for the 70-
472 mm \widehat{q}_{sat} -bin (2nd most probable) in the tropical western Pacific compiled using PR (2A25)
473 precipitation at 0.25° . This \widehat{q}_{sat} bin is chosen instead of the most probable bin (74.5 mm)
474 because for the latter, the 75-mm cap of TMIv7.1 CWV results in the CWV value relative to
475 critical being capped at ~ 11 mm, and hence the PDF of the highest CWV is missing. The same
476 joint-PDF is plotted in Fig. 7b on a log-log scale. Non-precipitating bins ($0 \leq P < 0.05 \text{ mm hr}^{-1}$)
477 aside, the joint-PDF is quantitatively similar across the \widehat{q}_{sat} range and ocean basins (Section S5).

478 For CWV below critical, the PDF in Fig. 7a drops sharply as P increases. As the CWV increases
479 and approaches critical, the PDF increases for all $P > 0$ with long tails extending into high
480 precipitation regime. This occurs until the CWV reaches critical, above which the PDF starts to
481 decrease, with a local PDF maximum developing at a positive P ($\sim 3 \text{ mm hr}^{-1}$) for the highest
482 CWV bin. From Figs. 7a and 7b (the same joint-PDF on different scales), there is not a clear
483 power-law or exponential dependence of the PDF on precipitation, although a possible
484 functional form will be discussed further below.

485 Note that the distribution of P is asymmetric, with the most probable value being (close to)
486 zero even for CWV around critical. As such, any Gaussian-like distribution (Lin and Neelin 2003)
487 or on-and-off precipitation model (Muller et al. 2009; Stechmann and Neelin 2014) with the
488 observed conditional mean and variance would miss much of the distribution details.

489 The radar-based precipitation retrievals are probably more reliable than the passive
490 microwave radiometer counterpart (including TMI) since the latter is based solely on a path-
491 integrated signal without phase information (Chen et al. 2013). The conditional precipitation
492 and probability of precipitation in Fig. 3 demonstrate that PR 2A25 and TMIv7.1 precipitation
493 are consistent in terms of the mean and distribution of low-to-moderate precipitation.
494 However, there are quantitative discrepancies for high precipitation between the two datasets.
495 Figure 7c shows the similar joint-PDF as in Fig. 7a, but using TMIv7.1 precipitation instead. In Fig.
496 7c, there is a clear cutoff at $P \sim 10 \text{ mm hr}^{-1}$ and practically no events for > 15 , despite the cap
497 set by the algorithm is 25. This is an undesirable characteristic of the retrieval algorithm when
498 applied to the Tropics (there is no sign of a cutoff in the extratropics; not shown). Besides the
499 cutoff, the joint-PDFs for $P < 10 \text{ mm hr}^{-1}$ are similar for PR and TMIv7.1, with minor quantitative
500 differences, e.g., the local PDF maximum at high CWV occurs at higher precipitation for TMIv7.1.
501 Thus, we shall not emphasize the distribution of precipitation from TMIv7.1 precipitation,
502 except for using it as an aid to study its dependence on spatial resolution.

503 Figure 8 shows the joint-PDF of CWV (relative to critical) and P compiled at different spatial
504 resolutions (details in caption). The two panels for 0.25° show the same joint-PDFs as in Figs. 7a
505 and 7c, but with a different CWV bin-width.

506 In terms of the general features, the joint-PDFs in Fig. 8 exhibit clear asymmetries between
507 the low-CWV—low-precipitation regime and regime near critical. However, in the vicinity of
508 critical (roughly $\pm 3 \text{ mm}$), the joint-PDFs are roughly symmetric with respect to CWV, consistent
509 with Figs. 2d and 2h. As CWV increases, the fraction of non-precipitating events decreases, as
510 indicated by the conditional probability of precipitation (orange dots; $P > 0$) and the bands at
511 the bottom for the top 3 panels (PDFs for $0 \leq P < 0.05 \text{ mm hr}^{-1}$). This and the extension of PDF
512 into high-precipitation around critical result in the sharp increase in the conditional mean (blue
513 solid line), median (white solid), and variance (blue dashed) of precipitation. These 3
514 conditional statistics, when calculated by excluding non-precipitating pixels, would still show a
515 sharp pickup around critical with slightly higher values for CWV below (not shown). Both the
516 precipitation distribution for $P > 0$ and its contrast to non-precipitating events (i.e., $P > 0$ vs. $P =$
517 0) contribute to the overall variance of precipitation (Stechmann and Neelin 2011).

518 In addition to the differences of PR and TMIv7.1 shown in Fig. 7, the conditional probability
519 for PR at 0.25° in Fig. 8 is noticeably higher than its TMIv7.1 counterpart for CWV lower than
520 critical, partly because of the differences in instrument sensitivity and native resolution of the

521 datasets. Recall in Fig. 3 that the conditional mean and probability (with respect to a different
522 1.05-mm hr⁻¹ threshold) from PR and TMIv7.1 are extremely close. Despite this, the two 0.25°
523 panels in Fig. 8 show that the TMIv7.1 precipitation tends to underestimate the variance of
524 precipitation for CWV around and above critical. Furthermore, the TMIv7.1 conditional median
525 approaches mean at high CWV, implying a more symmetric distribution of precipitation,
526 consistent with the corresponding PDFs in Fig. 7c.

527 As for the dependence on spatial resolution shown in Fig. 8, there are more weakly
528 precipitating events (e.g., $0 < P < 2$ mm hr⁻¹) in the expense of non-precipitating and heavily
529 precipitating events at lower resolutions, consistent with spatial-averaging, which also results in
530 the conditional probability increasing and variance decreasing with resolution.

531 Figure 9 shows the precipitation contribution as a function of CWV and P for the 70-mm
532 \widehat{q}_{sat} -bin in the tropical western Pacific on different scales. In Fig. 9a, the areas under the curve
533 integrated to the mean precipitation rate for this \widehat{q}_{sat} . While the largest contributions come
534 from near critical, values below or above critical still contribute substantially. The relatively
535 linear range in Fig. 9b appears to suggest that a $P^{-1}e^{-\beta P}$ dependence with $\beta \sim 0.16$ (mm hr⁻¹)⁻¹
536 might be a reasonable approximation for moderate to high precipitation for a wide range of
537 CWV. In both Figs. 9b and 9c, the value of P at which the precipitation contribution is a
538 maximum moves towards higher P as CWV increases.

539 Overall, the distributions of precipitation discussed in this section underline the importance
540 of considering the dependence of the precipitation PDF on where the CWV-temperature
541 environment is relative to critical, rather than as a single PDF for total precipitation.

542

543 **7. Summary and discussion**

544 In this work, the convective transition statistics over tropical oceans are compiled using
545 satellite retrievals and ARM site measurements to quantify the dependence of precipitation on
546 the water vapor and tropospheric temperature environment, and to provide an observational
547 baseline for comparison in using these statistics as model diagnostics at fast (convective)
548 timescales.

549 The mean tropospheric temperature profiles conditioned on precipitation ($P > 0.25$ mm hr⁻¹;
550 Fig. 4) show vertically coherent structure, justifying the use of bulk tropospheric temperature
551 measures like column-integrated saturation humidity \widehat{q}_{sat} , mass-weighted column average
552 temperature \widehat{T} , or other layered equivalents as the leading order description of temperature in
553 defining the convective transition statistics. Using these temperature measures yields
554 quantitatively similar statistics, e.g., those shown in Figs. 2-3, including the conditional

555 precipitation and probability of precipitation, critical CWV w_c , and PDFs of CWV for
556 precipitating events, though the PDFs of CWV for all events below critical may differ
557 significantly, reflecting the differences in the climatology of these temperature measures.
558 Because of the narrow temperature range in the tropics, the conversion among these
559 temperature measures can be carried out using simple linear relations found by regression.

560 Among the robust features of the precipitation-CWV relation is the conditional precipitation
561 as a function of CWV and tropospheric temperature, which is insensitive to spatial resolution
562 (Figs. 1-3) and time-averaging (Fig. 6), consistent with the assertion that the autocorrelation
563 spatial and temporal scales of CWV and temperature are much greater than that of
564 precipitation. This is particularly useful for model comparison since model output is subject to
565 varying spatial-temporal resolution. Because of this insensitivity, w_c and the slope α
566 characterizing the precipitation pickup are defined through the conditional precipitation. Both
567 w_c and α are approximately constant across ocean basins, with the latter being insensitive to
568 temperature over the most common range in the tropics. The dependence of the precipitation-
569 CWV relation on temperature is completely characterized by w_c in the sense that shifting CWV
570 by w_c collapses the convective transition statistics and the joint-PDFs of CWV and precipitation.
571 The dependence of w_c on temperature is, however, not a simple relation. Convective onset
572 occurs at higher CWV but at lower column relative humidity (CRH) with increasing temperature,
573 as noted in Neelin et al. (2009), and is consistent with the entraining plume calculations by
574 Sahany et al. (2012). At low temperatures, which lie along the subtropical margin of the domain,
575 critical values could plausibly be approximated by a constant CRH within a small regime. This
576 regime likely corresponds to the subtropical expression of mid-latitude frontal systems. For the
577 most common behavior in the tropical domain, we underline that using CRH as a variable,
578 without separately quantifying the water vapor-temperature dependence, would yield a poor
579 characterization of the statistics, as expected because of the dominance of conditional
580 instability as a source of tropical convective events.

581 Robustness of the presented statistics to instrumentation is examined by comparing various
582 datasets, including precipitation radar, microwave retrievals and in situ data. A major source of
583 uncertainty in the convective transition statistics is the measurement of CWV in the presence of
584 precipitation. Sensitivity to CWV gap-filling is quantified, which primarily affects probability
585 distributions at very high CWV (above critical). Despite the differences in precipitation
586 distribution, especially at high rain rate, associated with different datasets as indicated by the
587 joint-PDFs (Figs. 7-8), both conditional precipitation and probability of precipitation are robust
588 to instrumentation (including ground-based measurements of the former; Fig. 3). This
589 consistency likely reflects the calibration among precipitation datasets, and emphasizes the
590 reliability of these statistics as observational references for model diagnostics.

591 At the timescale of the individual retrieval, the tendency of precipitation to coincide with
592 high CWV has been observed. Here, this is quantified more precisely by including the
593 dependence on tropospheric temperature. Specifically, CWV relative to critical ($cwv - w_c$)
594 appears to be a useful predictor of precipitation over tropical oceans. Unlike the climatology of
595 precipitation or CWV that shows sharp contrast between major convergence zones and regions
596 elsewhere, the conditional probability of precipitation given CWV exceeding critical shows only
597 minor geographic variations (Fig. 5). In other words, the convective transition statistics created
598 from individual convective events conditioned on two bulk measures of the temperature—
599 water-vapor environment apply reasonably universally through the tropics even at the
600 individual space-time point. Small departures are noted that are presumably due to other
601 vertical degrees of freedom impacting convection. At larger spatial scales and sub-daily
602 timescales, events of high CWV relative to critical are almost certainly associated with
603 convection, leading to a potential application of using CWV above critical as a precipitation
604 predictor. A connection between above-critical events and mesoscale convective systems (Fig.
605 5e vs. TM09's Fig. 7) is noted, which could contribute to the robustness of conditional
606 precipitation to spatial resolution (up to $\sim 1^\circ$). A recent analysis of the GOAmazon campaign
607 data also points to the potential importance of organized flow in creating the dependence of
608 deep convection on lower tropospheric water vapor through a deep layer (Schiro et al. 2017)
609 that is seen here as the CWV dependence of precipitation.

610 It is common to discuss probability distributions of precipitation and to compare models to
611 these (e.g., Figs. 8 and 13 in Klingaman et al. 2017). However, the strong dependence of the
612 statistics on CWV relative to critical suggests that much of the important dynamics depend on
613 the temperature—water-vapor environment of the precipitating system. We extend the scope
614 of the precipitation-CWV relation to include the joint-PDF of CWV relative to critical and
615 precipitation rate P . This joint-PDF is quantitatively similar in the most common temperature
616 range across tropical ocean basins. For low CWV (relative to critical) the PDF drops rapidly as P
617 increases. As CWV increase, the PDF extends into high precipitation regime, and develops a
618 peak at a non-zero P ($\sim 3 \text{ mm hr}^{-1}$) for the highest CWV (Fig. 7a), with most of the precipitation
619 contribution from CWV around and above critical (mostly $P < 10 \text{ mm hr}^{-1}$; Fig. 9a).

620 Examination of the precipitation contributions suggests that the conditional distribution of
621 precipitation in the PR 2A25 data can be approximated by the functional form $P^{-1}e^{-\beta P}$ with β
622 $\sim 0.16 \text{ (mm hr}^{-1}\text{)}^{-1}$ for sufficiently high P , for a wide range of CWV (Fig. 9b). This would
623 correspond to a gamma distribution at the limit of its range of validity, except that there is a
624 clear low-precipitation cutoff in the precipitation contribution that changes systematically as a
625 function of CWV above critical. This apparently simple observational relationship in
626 precipitation distributions as a function of CWV relative to critical can potentially provide an
627 interesting target for theoretical work.

628 The joint-PDF does exhibit dependence on spatial averaging, with the joint-PDF exhibiting
629 more light precipitation at the expense of non-precipitating and heavily precipitating events, at
630 lower spatial resolution (Fig. 8). This resolution dependence results in the dependence of
631 conditional probability of precipitation on resolution, as in Figs. 1-3. There is not enough
632 observational data to compile the joint-PDF at resolutions most common for current models (\sim
633 1°) without losing information for the highest CWV, but qualitative dependence of the joint-PDF
634 on distance above critical can be used as an auxiliary diagnostic tool for the evaluation of
635 modeled convective parameterizations.

636 Overall, in addition to providing an observational baseline with quantified robustness and
637 resolution dependence of the basic convective transition statistics for model comparison, the
638 ability to summarize statistics in terms of CWV relative to critical enables additional diagnostics.
639 The dependence of precipitation probability on this quantity expands the set of related
640 properties that exhibit common behavior for precipitation throughout the tropics.

641

Acknowledgements

642 This research was supported by National Oceanic and Atmospheric Administration Grants
643 NA15OAR4310097 and NA14OAR4310274, the Office of Biological and Environmental Research
644 of the U.S. Department of Energy Grant DE-SC0011074, and National Science Foundation Grant
645 AGS-1540518. U.S. Department of Energy Atmospheric Radiation Measurement (ARM) Climate
646 Research Facility GOAmazon and tropical western Pacific field campaign data are acknowledged.
647 We thank J. Meyerson for graphical assistance. A portion of this work has previously been
648 presented at an American Geophysical Union meeting (Kuo et al. 2016). The authors thank Dr.
649 M. W. Moncrieff and an anonymous reviewer for insightful review comments.

650

References

- 651 Ahmed, F., and C. Schumacher, 2017: Geographical differences in the tropical precipitation-
652 moisture relationship and rain intensity onset. *Geophys. Res. Lett.*, **44**(2), 1114-1122.
- 653 Atmospheric Radiation Measurement (ARM) Climate Research Facility. 1996, updated hourly.
654 MWR Retrievals (MWRRET1LILJCLOU). 1998-01-01 to 2010-12-31, Tropical Western Pacific
655 (TWP) Central Facility, Manus I., PNG (C1). Compiled by K. Gaustad and L. Riihimaki.
656 Atmospheric Radiation Measurement (ARM) Climate Research Facility Data Archive: Oak
657 Ridge, Tennessee, USA. Data set accessed 2016 at <http://dx.doi.org/10.5439/1027369>.
- 658 Atmospheric Radiation Measurement (ARM) Climate Research Facility. 1997, updated hourly.
659 Surface Meteorological Instrumentation (MET). 1998-01-01 to 2010-12-31, Tropical Western
660 Pacific (TWP) Central Facility, Manus I., PNG (C1). Compiled by D. Holdridge and J. Kyrouac.
661 Atmospheric Radiation Measurement (ARM) Climate Research Facility Data Archive: Oak
662 Ridge, Tennessee, USA. Data set accessed 2016 at <http://dx.doi.org/10.5439/1025220>.
- 663 Atmospheric Radiation Measurement (ARM) Climate Research Facility. 1998, updated hourly.
664 Surface Meteorological Instrumentation (MET). 1999-01-01 to 2008-12-31, Tropical Western
665 Pacific (TWP) Central Facility, Nauru Island (C2). Compiled by D. Holdridge and J. Kyrouac.
666 Atmospheric Radiation Measurement (ARM) Climate Research Facility Data Archive: Oak
667 Ridge, Tennessee, USA. Data set accessed 2016 at <http://dx.doi.org/10.5439/1025220>.
- 668 Atmospheric Radiation Measurement (ARM) Climate Research Facility. 1998, updated hourly.
669 MWR Retrievals (MWRRET1LILJCLOU). 1999-01-01 to 2008-12-31, Tropical Western Pacific
670 (TWP) Central Facility, Nauru Island (C2). Compiled by K. Gaustad and L. Riihimaki.
671 Atmospheric Radiation Measurement (ARM) Climate Research Facility Data Archive: Oak
672 Ridge, Tennessee, USA. Data set accessed 2016 at <http://dx.doi.org/10.5439/1027369>.
- 673 Benedict, J. J., E. D. Maloney, A. H. Sobel, D. M. W. Frierson, and L. J. Donner, 2013: Tropical
674 intraseasonal variability in version 3 of the GFDL atmosphere model. *J. Climate*, **26**, 426-449,
675 doi:10.1175/JCLI-D-12-00103.1.
- 676 Benedict, J. J., E. D. Maloney, A. H. Sobel, and D. M. W. Frierson, 2014: Gross moist stability and
677 MJO simulation skill in three full-physics GCMs. *J. Atmos. Sci.*, **71**, 3327-3349,
678 doi:10.1175/JAS-D-13-0240.1.
- 679 Bergemann, M., and C. Jakob, 2016: How important is tropospheric humidity for coastal rainfall
680 in the tropics? *Geophys. Res. Lett.*, **43**(11), 5860-5868.

681 Bernstein, D. N., and J. D. Neelin, 2016: Identifying sensitive ranges in global warming
682 precipitation change dependence on convective parameters. *Geophys. Res. Lett.*, **43**(11),
683 5841-5850.

684 Booth, J. F., Y.-O. Kwon, S. Ko, R. J., Small, and R. Msadek, 2017: Spatial Patterns and Intensity
685 of the Surface Storm Tracks in CMIP5 Models, *J. Climate*, **30**, 4965-4981, doi:10.1175/JCLI-D-
686 16-0228.1.

687 Boyle, J. S., S. A. Klein, D. D. Lucas, H.-Y., Ma, J. Tannahill, and S. Xie, 2015: The parametric
688 sensitivity of CAM5's MJO. *J. Geophys. Res. Atmos.*, **120**, 1424-1444,
689 doi:10.1002/2014JD022507.

690 Bretherton, C. S., M. E. Peters, and L. E. Back, 2004: Relationships between water vapor path
691 and precipitation over the tropical oceans. *J. Climate*, **17**(7), 1517-1528.

692 Brown, R. G., and C. Zhang, 1997: Variability of midtropospheric moisture and its effect on
693 cloud-top height distribution during TOGA COARE. *J. Atmos. Sci.*, **54**(23), 2760-2774.

694 Camargo, S. J., M. K. Tippett, A. H. Sobel, G. A. Vecchi, and M. Zhao, 2014: Testing the
695 performance of tropical cyclone genesis indices in future climates using the HiRAM model. *J.*
696 *Climate*, **27**, 9171-9196.

697 Chen, Y., E. E. Ebert, K. J. E. Walsh, and N. E. Davidson, 2013: Evaluation of TRMM 3B42
698 precipitation estimates of tropical cyclone rainfall using PACRAIN data. *J. Geophys. Res.*
699 *Atmos.*, **118**, 2184-2196, doi:10.1002/jgrd.50250.

700 Chen, D., and A. Dai, 2017: Dependence of estimated precipitation frequency and intensity on
701 data resolution. *Clim. Dyn.*, doi:10.1007/s00382-017-3830-7.

702 Covey, C., P. J. Gleckler, C. Doutriaux, D. N. Williams, A. Dai, J. Fasullo, K. Trenberth, and A. Berg,
703 2016: Metrics for the Diurnal Cycle of Precipitation: Toward Routine Benchmarks for Climate
704 Models, *J. Climate*, **29**, 4461-4471, doi:10.1175/JCLI-D-15-0664.1.

705 Derbyshire, S. H., I. Beau, P. Bechtold, J. Y. Grandpeix, J. M. Piriou, J. L. Redelsperger, and P. M.
706 M. Soares, 2004: Sensitivity of moist convection to environmental humidity. *Quart. J. Roy.*
707 *Meteor. Soc.*, **130**(604), 3055-3079.

708 Gonzalez, A., and X. Jiang, 2017: Winter Mean Lower-Tropospheric Moisture over the Maritime
709 Continent as a Climate Model Diagnostic Metric for the Propagation of the Madden-Julian
710 Oscillation. *Geophys. Res. Lett.*, **44**, doi:10.1002/2016GL072430.

711 Hirota, H., Y. N. Takayabu, M. Watanabe, M. Kimoto, and M. Chikira, 2014: Role of Convective
712 Entrainment in Spatial Distributions of and Temporal Variations in Precipitation over Tropical
713 Oceans. *J. Climate*, **27**, 8707-8723.

714 Holloway, C. E., and J. D. Neelin, 2007: The convective cold top and quasi equilibrium. *J. Atmos.*
715 *Sci.*, **64**, 1467-1487, doi:10.1175/JAS3907.1.

716 Holloway, C. E., and J. D. Neelin, 2009: Moisture vertical structure, column water vapor, and
717 tropical deep convection. *J. Atmos. Sci.*, **66**(6), 1665-1683.

718 Jiang, X., M. Zhao, E. Maloney, and D. E. Waliser, 2016: Convective Moisture Adjustment Time-
719 scale as a Key Factor in Regulating Model Amplitude of the Madden-Julian Oscillation,
720 *Geophys. Res. Lett.*, **43**, doi:10.1002/2016GL070898.

721 Jiang, X., 2017: Key processes for the eastward propagation of the Madden-Julian Oscillation
722 based on multi-model simulations. *J. Geophys. Res. Atmos.*, **122**, doi:10.1002/2016JD025955.

723 Kanamitsu, M., and Coauthors, 2002: NCEP/DOE AMIP-II Reanalysis (R-2). *Bull. Amer. Meteor.*
724 *Soc.*, **83**, 1631-1643.

725 Kim, D., and Coauthors, 2014: Process-oriented MJO simulation diagnostic: Moisture sensitivity
726 of simulated convection. *J. Climate*, **27**, 5379–5395, doi:10.1175/JCLI-D-13-00497.1.

727 Klingaman, N. P., G. M. Martin, and A. Moise, 2017: ASoP (v1.0): a set of methods for analyzing
728 scales of precipitation in general circulation models. *Geosci. Model Dev.*, **10**, 57-83,
729 doi:10.5194/gmd-10-57-2017.

730 Kodama, C., and Coauthors, 2015: A 20-Year Climatology of a NICAM AMIP-Type Simulation, *J.*
731 *Meteor. Soc. Japan*, **93**, 393-424, doi:https://doi.org/10.2151/jmsj.2015-024.

732 Kuo, Y.-H., and Coauthors, 2016: Convective transition statistics for climate model diagnostics.
733 Abstract A13L-03 presented at 2016 Fall Meeting, AGU, San Francisco, Calif., 12-16 Dec.

734 Kuo, Y.-H., J. D. Neelin, and C. R. Mechoso, 2017: Tropical Convective Transition Statistics and
735 Causality in the Water Vapor-Precipitation Relation. *J. Atmos. Sci.*, **74**(3), 915-931.

736 Langenbrunner, B., and J. D. Neelin: Multiobjective constraints for climate model parameter
737 choices: Pragmatic Pareto fronts in CESM1. *J. Adv. Model. Earth Syst.*, accepted,
738 doi:10.1002/2017MS000942.

739 Lin, J. W.-B., and J. D. Neelin, 2003: Toward stochastic deep convective parameterization in
740 general circulation models. *Geophys. Res. Lett.*, **30**, doi:10.1029/2002GL016203.

741 Mapes, B., S. Tulich, J. Lin, and P. Zuidema, 2006: The mesoscale convection life cycle: Building
742 block or prototype for largescale tropical waves? *Dyn. Atmos. Oceans*, **42**, 3-29,
743 doi:10.1016/j.dynatmoce.2006.03.003.

744 Mapes, B., and R. Neale, 2011: Parameterizing convective organization to escape the
745 entrainment dilemma. *J. Adv. Model. Earth Syst.*, **3**, M06004, doi:10.1029/2011MS000042.

746 Moncrieff, M. W., C. Liu, and P. Bogenschutz, 2017: Simulation, modeling, and dynamically
747 based parameterization of organized tropical convection for global climate models. *J. Atmos.*
748 *Sci.*, **74**(5), 1363-1380.

749 Muller, C. J., L. E. Back, P. A. O’Gorman, and K. A. Emanuel, 2009: A model for the relationship
750 between tropical precipitation and column water vapor. *Geophys. Res. Lett.*, **36**,
751 doi:10.1029/2009GL039667.

752 Neelin, J. D., O. Peters, and K. Hales, 2009: The transition to strong convection. *J. Atmos.*
753 *Sci.*, **66**(8), 2367-2384.

754 Oueslati, B., and G. Bellon, 2011: Convective entrainment and large-scale organization of
755 tropical precipitation: Sensitivity of the CNRM-CM5 hierarchy of models. *J. Climate*, **26**(9),
756 2931-2946.

757 Parsons, D. B., J.-L. Redelsperger, and K. Yoneyama, 2000: The evolution of the tropical western
758 Pacific atmosphere-ocean system following the arrival of a dry intrusion. *Quart. J. Roy.*
759 *Meteor. Soc.*, **126**(563), 517-548.

760 Peters, O., and J. D. Neelin, 2006: Critical phenomena in atmospheric precipitation. *Nat. Phys.*, **2**,
761 393-396.

762 Redelsperger, J. L., D. B. Parsons, and F. Guichard, 2002: Recovery processes and factors limiting
763 cloud-top height following the arrival of a dry intrusion observed during TOGA COARE. *J.*
764 *Atmos. Sci.*, **59**(16), 2438-2457.

765 Ridout, J. A, 2002: Sensitivity of tropical Pacific convection to dry layers at mid-to upper levels:
766 Simulation and parameterization tests. *J. Atmos. Sci.*, **59**(23), 3362-3381.

767 Rowell, D. P., 2012: Sources of uncertainty in future changes in local precipitation. *Clim. Dyn.*,
768 **39**, 1929-1950, doi:10.1007/s00382-011-1210-2.

769 Rushley, S. S., D. Kim, C. S. Bretherton, and M.-S. Ahn, 2018: Reexamining the Nonlinear
770 Moisture-Precipitation Relationship Over the Tropical Oceans. *Geophys. Res. Lett.*, **45**,
771 doi:10.1002/2017GL076296.

772 Sahany, S., J. D. Neelin, K. Hales, and R. B. Neale. 2012: Temperature-moisture dependence of
773 the deep convective transition as a constraint on entrainment in climate models. *J. Atmos.*
774 *Sci.*, **69**(4), 1340-1358.

775 Sahany, S., J. D. Neelin, K. Hales, and R. B. Neale, 2014: Deep convective transition
776 characteristics in the Community Climate System Model and changes under global warming. *J.*
777 *Climate*, **27**(24), 9214-9232.

778 Sanderson, B. M., 2011: A multimodel study of parametric uncertainty in predictions of climate
779 response to rising greenhouse gas concentrations. *J. Climate*, **25**, 1362-1377.

780 Schiro, K. A., J. D. Neelin, D. K. Adams, and B. R. Lintner, 2016: Deep convection and column
781 water vapor over tropical land versus tropical ocean: A comparison between the Amazon and
782 the tropical western Pacific. *J. Atmos. Sci.*, **73**(10), 4043-4063.

783 Schiro, K. A., F. Ahmed, and J. D. Neelin, 2017: GoAmazon2014/5 campaign points to deep-
784 inflow approach to mesoscale-organized and unorganized deep convection. Submitted.

785 Sherwood, S. C., and R. Wahrlich, 1999: Observed evolution of tropical deep convective events
786 and their environment. *Mon. Wea. Rev.*, **127**(8), 1777-1795.

787 Sherwood, S. C., S. Bony, and J.-L. Dufresne, 2014: Spread in model climate sensitivity traced to
788 atmospheric convective mixing. *Nature*, **505**(7481), 37-42.

789 Stechmann, S. N., and J. D. Neelin, 2011: A stochastic model for the transition to strong
790 convection. *J. Atmos. Sci.*, **68**(12), 2955-2970.

791 Stechmann, S. N., and J. D. Neelin, 2014: First-passage-time prototypes for precipitation
792 statistics. *J. Atmos. Sci.*, **71**(9), 3269-3291.

793 Tao, W.-K. and M. W. Moncrieff, 2009: Multiscale cloud system modeling. *Rev. Geophys.*, **47**,
794 RG4002, doi:10.1029/2008RG000276.

795 Tompkins, A. M, 2001: Organization of tropical convection in low vertical wind shears: The role
796 of water vapor. *J. Atmos. Sci.*, **58**(6), 529-545.

797 Torri, G., Z. Kuang, and Y. Tian, 2015: Mechanisms for convection triggering by cold pools.
798 *Geophys. Res. Lett.*, **42**, doi:10.1002/2015GL063227.

799 Tropical Rainfall Measuring Mission (TRMM) (2011), TRMM Precipitation Radar Rainfall Rate
800 and Profile L2 1.5 hours V7, Greenbelt, MD, Goddard Earth Sciences Data and Information
801 Services Center (GES DISC), Accessed 19 Aug 2016
802 https://disc.gsfc.nasa.gov/datacollection/TRMM_2A25_7.html

803 Tropical Rainfall Measuring Mission (TRMM) (2011), TRMM (TMPA) Rainfall Estimate L3 3 hour
804 0.25 degree x 0.25 degree V7, Greenbelt, MD, Goddard Earth Sciences Data and Information
805 Services Center (GES DISC), Accessed 08 Jul 2016
806 https://disc.gsfc.nasa.gov/datacollection/TRMM_3B42_7.html

807 University of Wyoming Atmospheric Soundings, Accessed 21 August 2017
808 <http://weather.uwyo.edu/upperair/sounding.html>.

- 809 Wentz, F.J., C. Gentemann, K.A. Hilburn, 2015: Remote Sensing Systems TRMM TMI Daily
810 Environmental Suite on 0.25 deg grid, Version 7.1. Remote Sensing Systems, Santa Rosa, CA.
811 Available online at www.remss.com/missions/tmi. Accessed 08 Jul 2016.
- 812 Yano, J.-I., C. Liu, and M. W. Moncrieff, 2012: Self-organized criticality and homeostasis in
813 atmospheric convective organization. *J. Atmos. Sci.*, **69**, 3449-3462, doi:10.1175/JAS-D-12-
814 069.1.
- 815 Yokohata, T., J. D. Annan, M. Collins, C. S. Jackson, M. Tobis, M. Webb, and J. C. Hargreaves,
816 2012: Reliability of multi-model and structurally different single-model ensembles. *Clim.*
817 *Dyn.*, **39**, 599-616.

Figure captions

819 **Figure 1:** (a) Conditionally averaged precipitation rate; (b) conditional probability of
 820 precipitation; (c) probability density function of all events, and (d) precipitating events only as a
 821 function of CWV and \widehat{q}_{sat} (units: mm) for the tropical (20°S-20°N) western Pacific. (e)-(h) Same
 822 statistics, but for the tropical eastern Pacific, (i)-(l) for Atlantic, and (m)-(p) for Indian Ocean.
 823 Results are shown using TMIv7.1 data and Reanalysis-2 temperature compiled at 0.25° (colored
 824 markers) and 0.5° (dots). Underpopulated bins at 0.25° (PDF < 10⁻⁵) are indicated by open
 825 circles, and those for 0.5° are omitted. Triangles represent the corresponding \widehat{q}_{sat} values. Here,
 826 precipitating events are defined by $P > 1.05 \text{ mm hr}^{-1}$. The CWV data is gap-filled using nearest
 827 available values, and data from pixels within 2.5° of land are excluded to avoid potentially
 828 erroneous temperature values arising from spatial interpolation. The standard errors associated
 829 with the conditional precipitation are smaller than the marker size, and omitted. The
 830 corresponding statistics compiled using \widehat{T} as the bulk tropospheric temperature measure are
 831 plotted in Fig. S4.

832 **Figure 2:** (a)-(d) Convective transition statistics for the tropical western Pacific as in Figs. 1a-1d
 833 for 0.25° (colored markers) and 0.5° (dots), but for each marker/dot shifted by the
 834 corresponding critical CWV (w_c) from Fig. 3c, and with PDFs scaled. The best-fit for conditional
 835 precipitation is shown as gray line in (a), with its slope indicated by α . (e)-(h) Same as (a)-(d),
 836 but using \widehat{T} instead of \widehat{q}_{sat} as the bulk tropospheric temperature measure. The colored
 837 triangles represent average \widehat{q}_{sat} conditioned on \widehat{T} and CRH ($\equiv \text{CWV}/\widehat{q}_{sat}$) > 60%, shifted by w_c .
 838 The corresponding plots for the other basins are in Figs. S5 and S6.

839 **Figure 3:** (a) Collapsed conditional precipitation and (b) probability of precipitation; (c) critical
 840 CWV w_c and (d) critical CRH ($\equiv w_c/\widehat{q}_{sat}$) for tropical oceans using \widehat{q}_{sat} as the bulk tropospheric
 841 temperature measure. (e)-(h) Same as (a)-(d), but using \widehat{T} instead of \widehat{q}_{sat} as the bulk
 842 temperature. The conditional precipitation [(a), (e)] and probability of precipitation [(b), (f); $P >$
 843 1.05 mm hr^{-1}] are compiled for 3 combinations of datasets: (i) TMIv7.1 CWV and precipitation
 844 (colored dots) with underpopulated bins plotted as open circles, (ii) TMIv7.1 CWV and PR 2A25
 845 precipitation (gray dots) excluding underpopulated bins, and (iii) ARM site CWV and
 846 precipitation measurements from Manus (diamonds) and Nauru (squares) Islands in the tropical
 847 western Pacific (WPac). Reanalysis-2 temperature is used for (i)-(iii). For (i) and (ii), bins from all
 848 four basins are plotted, with data at 0.25° resolution and coastal regions excluded. For (iii), the
 849 CWV values are shifted by the corresponding w_c given the temperature (\widehat{q}_{sat} or \widehat{T}) time series
 850 according the w_c -temperature relation for WPac [as in (c) and (g)]. The critical CWV [(c), (g)]
 851 and critical CRH [(d), (h)] are calculated for combinations (i) and (ii), respectively. The colored
 852 solid lines in (c) and (g) represent \widehat{q}_{sat} conditioned on temperature and CRH ($\equiv \text{CWV}/\widehat{q}_{sat}$) > 60%.

853 This conditional \widehat{q}_{sat} is also used in defining the critical CRH. The gray lines in (c) represent CRH
854 from 100% to 80% with 2% spacing.

855 **Figure 4:** Reanalysis-2 temperature profiles conditionally averaged on TMIv7.1 precipitation and
856 \widehat{q}_{sat} . Profiles are anomalies with respect to the mean profile averaged over all precipitating
857 events ($P > 0.25 \text{ mm hr}^{-1}$) with coastal regions excluded.

858 **Figure 5:** (a) The probability of precipitation as a function of geographical location, calculated
859 using TMIv7.1 precipitation at 0.25° resolution. (b) The conditional probability of precipitation
860 given CWV exceeding critical, calculated using TMIv7.1 CWV and precipitation, and Reanalysis-2
861 temperature at 0.25° . Here the conditional probability is calculated from the frequency binned
862 by $cwv - w_c(\widehat{q}_{sat})$, P , and geographical location, with $w_c(\widehat{q}_{sat})$ as in Fig. 3c averaged over four
863 basins. (c) Same as in (b) but at 1° . (d) Same as in (b), but with P defined as the maximum of the
864 TMIv7.1 precipitation rate and two additional 3B42 precipitation rates that are closest in time
865 to the TMIv7.1 measurement. (e) The fraction of total precipitation from events with CWV
866 exceeding critical, calculated using data as in (b) at 0.25° . (f) Precipitation rate (for $P \geq 0.25 \text{ mm}$
867 hr^{-1}) on top of regions of CWV exceeding critical using TMIv7.1 data at 1° for ascending orbits
868 on 01 Jan 2004. Note that (f) is a realization of the conditional probability in (c) on a particular
869 day. For (a)-(e), the precipitation threshold 0.25 mm hr^{-1} is chosen for comparison across spatial
870 resolution, and CWV offset -1.5 mm to include more events. The magnitudes of
871 probabilities/fraction in these panels depend on the precipitation threshold and CWV offset,
872 while the corresponding geographic patterns appear to be robust.

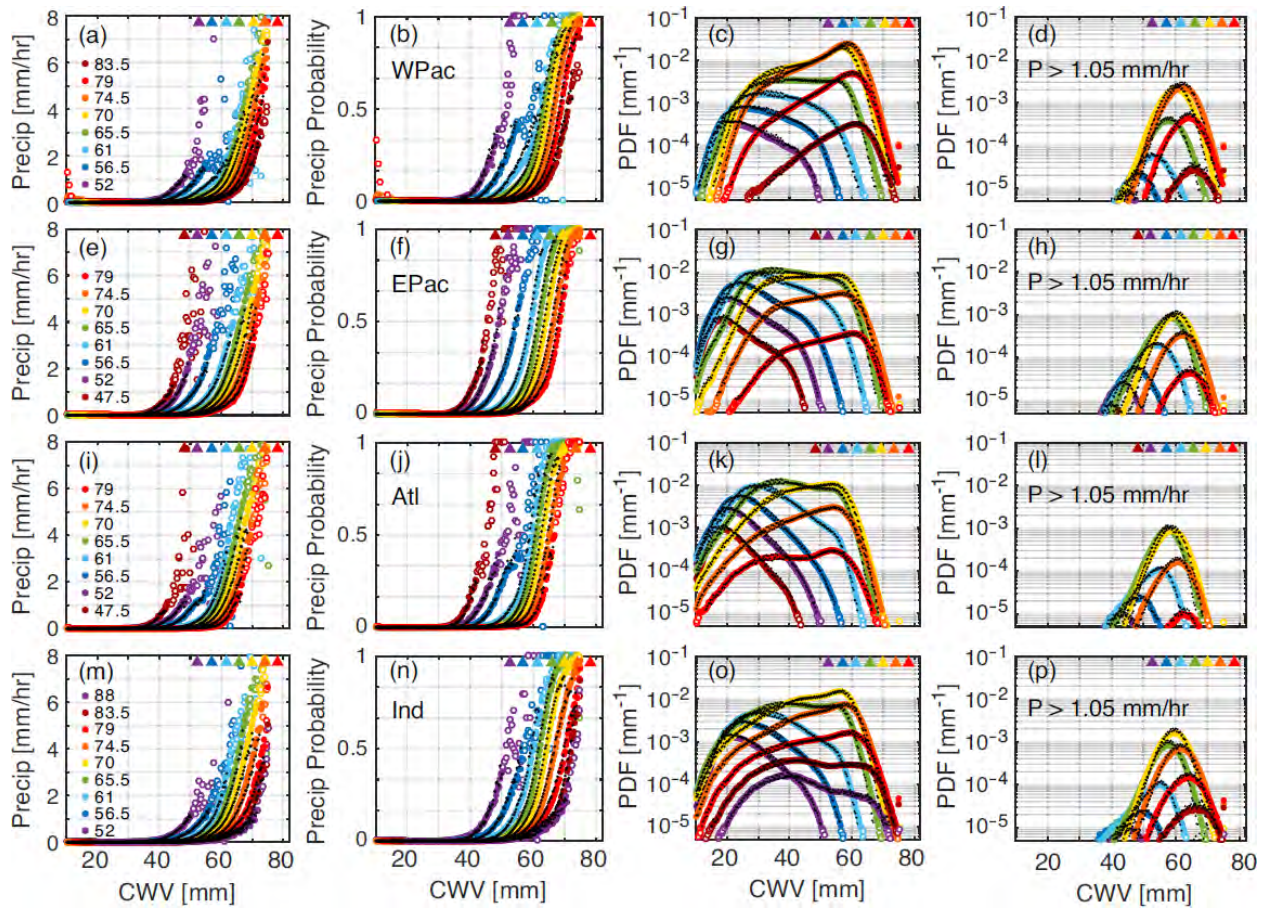
873 **Figure 6:** (Left) Precipitation rate with standard error as error bar, (center) probability of
874 precipitation $P > 0.5 \text{ mm hr}^{-1}$, and (right) frequency density of all events (crosses) and
875 precipitating events (circles), all conditioned on CWV using ARM site microwave radiometer
876 CWV and precipitation data for the GOAmazon site in the Amazon (top), and for Nauru (middle)
877 and Manus (bottom) Islands in the tropical western Pacific. Here the statistics are calculated
878 using CWV and precipitation data time-averaged at 15-min (dark red), 1-hr (red), 3-hr (yellow),
879 6-hr (green), and 24-hr (blue) intervals. Conditional precipitation without error bar indicates a
880 standard error smaller than the marker size.

881 **Figure 7:** (a) Joint-PDF of CWV relative to critical and precipitation rate P for the 70-mm \widehat{q}_{sat} -
882 bin in the tropical western Pacific compiled using TMIv7.1 CWV, Reanalysis-2 temperature and
883 PR 2A25 precipitation at 0.25° by treating CWV and P as continuous variables with bin-width 3
884 mm, and 0.1 mm hr^{-1} (0.05 for lowest bin), respectively. (b) Same as in (a), but on a log-log scale.
885 (c) Same as in (a), but using TMIv7.1 precipitation (0.25°). The colors indicate the values of CWV
886 relative to w_c .

887 **Figure 8:** Color shading: Joint-PDF (units: $\text{mm}^{-2} \text{hr}$), on a \log_{10} -scale, of CWV relative to critical
888 and precipitation rate P for the 70-mm \widehat{q}_{sat} -bin in the tropical western Pacific compiled using
889 TMIv7.1 CWV and Reanalysis-2 temperature, PR 2A25 (at 5 km and 0.25°) and TMIv7.1 (at 0.25° ,
890 0.5° , and 1°) precipitation, by treating CWV and P as continuous variables. The spacing between
891 the joint-PDF contours is 0.3, i.e., the color advances whenever the joint-PDF doubles ($10^{0.3} \sim 2$).
892 The corresponding precipitation rate (blue solid line), probability of precipitation ($P > 0 \text{ mm hr}^{-1}$;
893 orange dots), median (white solid line) and variance (blue dashed line) of precipitation, all
894 conditioned on CWV, are also shown for reference. For PR (at 5 km and 0.25°) and TMIv7.1
895 (0.25°), the bands at the bottom indicate bins with $0 \leq P < 0.05 \text{ mm hr}^{-1}$. Note that the
896 minimum nonzero P for raw PR data at 5 km is $\sim 0.11 \text{ mm hr}^{-1}$, and the TMIv7.1 precipitation at
897 0.25° is discretized with units 0.1 mm hr^{-1} .

898 **Figure 9:** Precipitation rate-weighted Joint-PDF of CWV relative to critical and precipitation rate
899 P , i.e., the precipitation contribution as a function of CWV and P , for the 70-mm \widehat{q}_{sat} -bin in the
900 tropical western Pacific. (a) linear axes; (b) log-linear axes; (c) log-log axes. The data correspond
901 to the Joint-PDF of CWV relative to critical and P in Fig. 7a, using PR 2A25 precipitation at 0.25° .
902 The colors indicate the values of CWV relative to w_c .

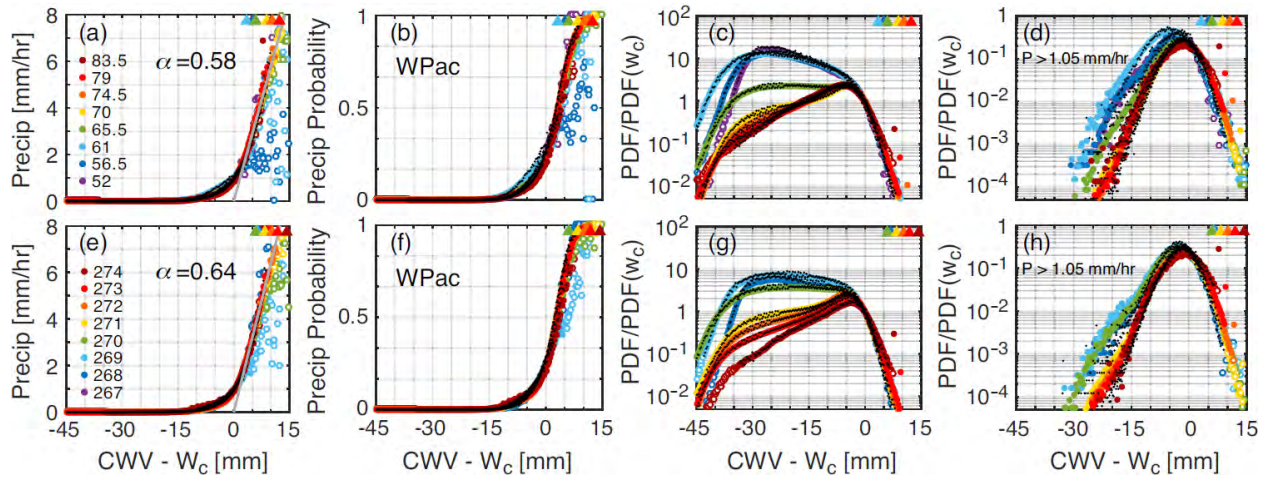
903



904

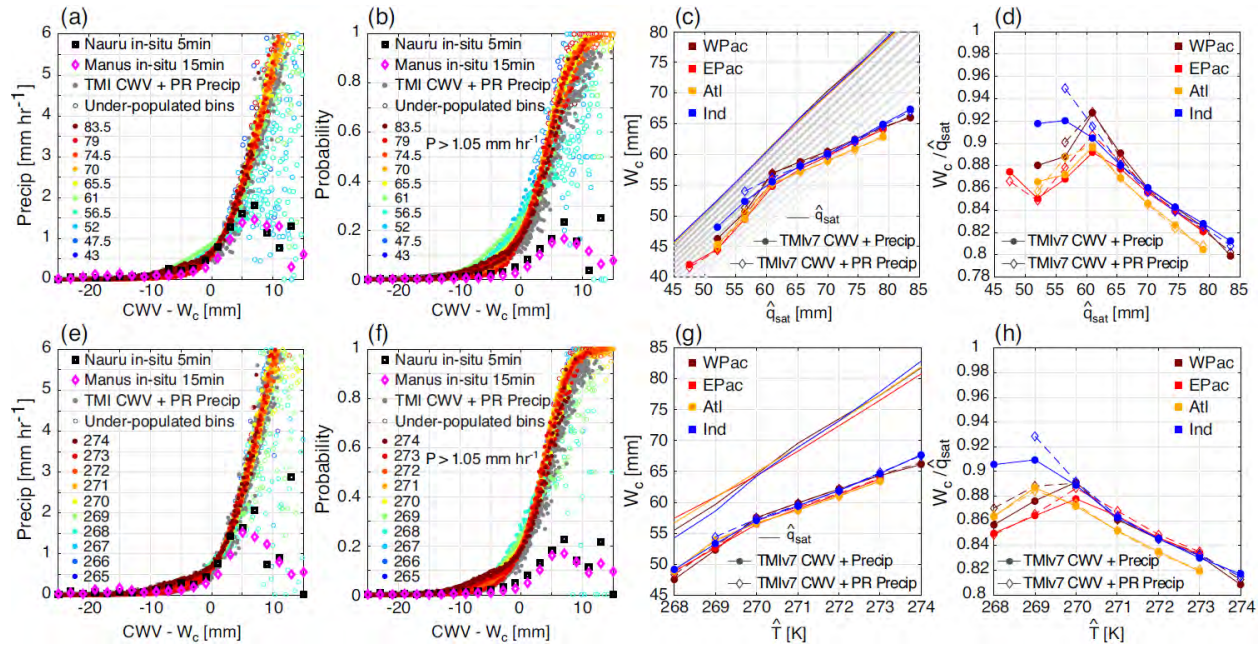
905 **Figure 1:** (a) Conditionally averaged precipitation rate; (b) conditional probability of precipitation; (c)
 906 probability density function of all events, and (d) precipitating events only as a function of CWV and \widehat{q}_{sat}
 907 (units: mm) for the tropical (20°S-20°N) western Pacific. (e)-(h) Same statistics, but for the tropical
 908 eastern Pacific, (i)-(l) for Atlantic, and (m)-(p) for Indian Ocean. Results are shown using TMIv7.1 data
 909 and Reanalysis-2 temperature compiled at 0.25° (colored markers) and 0.5° (dots). Underpopulated bins
 910 at 0.25° (PDF < 10⁻⁵) are indicated by open circles, and those for 0.5° are omitted. Triangles represent
 911 the corresponding \widehat{q}_{sat} values. Here, precipitating events are defined by $P > 1.05 \text{ mm hr}^{-1}$. The CWV
 912 data is gap-filled using nearest available values, and data from pixels within 2.5° of land are excluded to
 913 avoid potentially erroneous temperature values arising from spatial interpolation. The standard errors
 914 associated with the conditional precipitation are smaller than the marker size, and omitted. The
 915 corresponding statistics compiled using \widehat{T} as the bulk tropospheric temperature measure are plotted in
 916 Fig. S4.

917



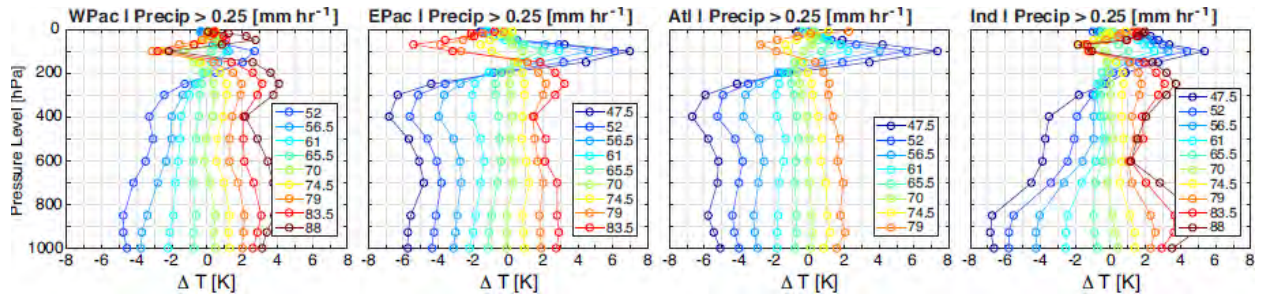
918

919 **Figure 2:** (a)-(d) Convective transition statistics for the tropical western Pacific as in Figs. 1a-1d for 0.25°
 920 (colored markers) and 0.5° (dots), but for each marker/dot shifted by the corresponding critical CWV
 921 $w_c(\widehat{q}_{sat})$ from Fig. 3c, and with PDFs scaled. The best-fit for conditional precipitation is shown as gray
 922 line in (a), with its slope indicated by α . (e)-(h) Same as (a)-(d), but using \widehat{T} instead of \widehat{q}_{sat} as the bulk
 923 tropospheric temperature measure. The colored triangles represent average \widehat{q}_{sat} conditioned on \widehat{T} and
 924 CRH ($\equiv CWV/\widehat{q}_{sat}$) > 60%, shifted by w_c . The corresponding plots for the other basins are in Figs. S5 and
 925 S6.



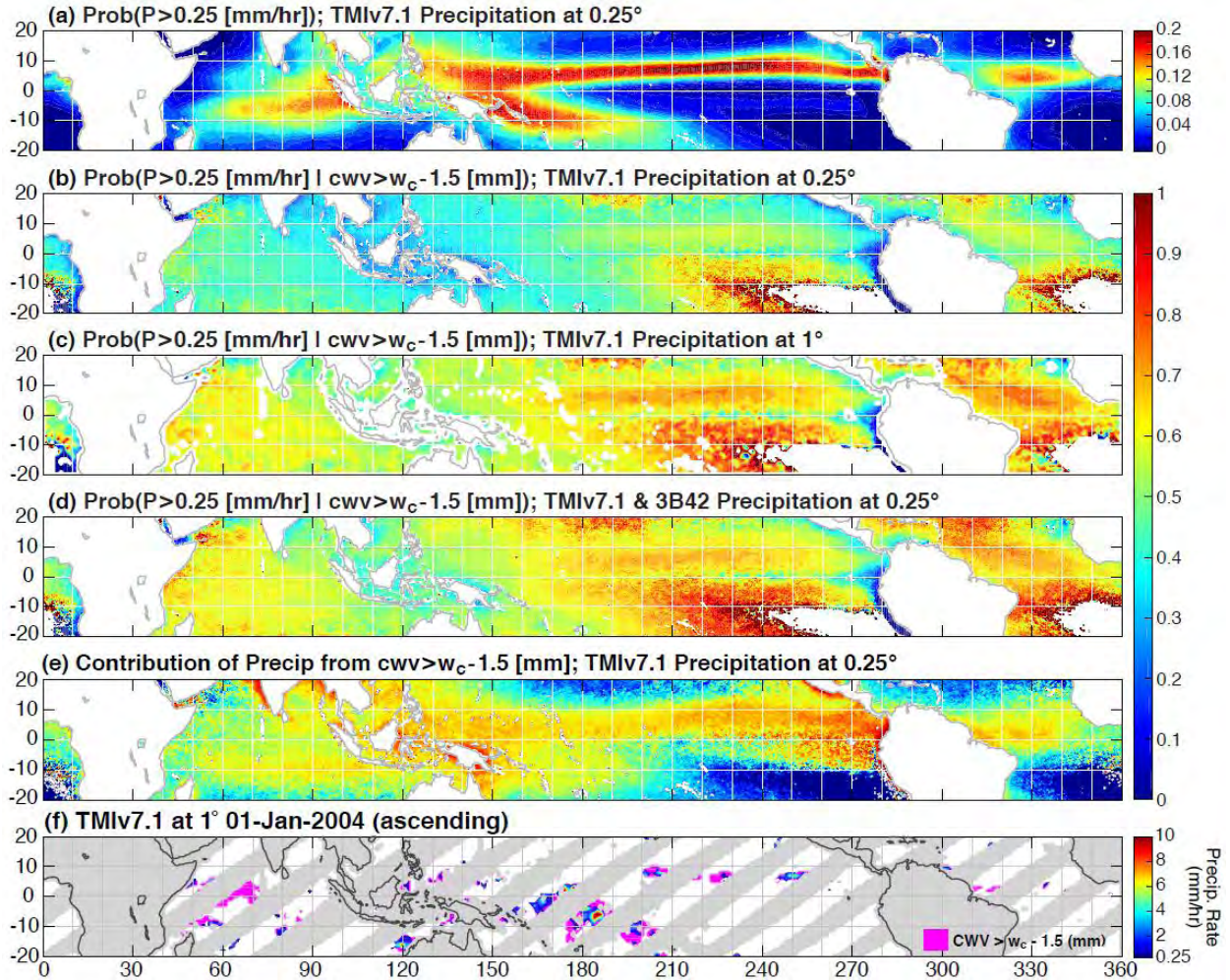
927

928 **Figure 3:** (a) Collapsed conditional precipitation and (b) probability of precipitation; (c) critical CWV w_c
 929 and (d) critical CRH ($\equiv w_c / \hat{q}_{sat}$) for tropical oceans using \hat{q}_{sat} as the bulk tropospheric temperature
 930 measure. (e)-(h) Same as (a)-(d), but using \hat{T} instead of \hat{q}_{sat} as the bulk temperature. The conditional
 931 precipitation [(a), (e)] and probability of precipitation [(b), (f); $P > 1.05 \text{ mm hr}^{-1}$] are compiled for 3
 932 combinations of datasets: (i) TMIv7.1 CWV and precipitation (colored dots) with underpopulated bins
 933 plotted as open circles, (ii) TMIv7.1 CWV and PR 2A25 precipitation (gray dots) excluding
 934 underpopulated bins, and (iii) ARM site CWV and precipitation measurements from Manus (diamonds)
 935 and Nauru (squares) Islands in the tropical western Pacific (WPac). Reanalysis-2 temperature is used for
 936 (i)-(iii). For (i) and (ii), bins from all four basins are plotted, with data at 0.25° resolution and coastal
 937 regions excluded. For (iii), the CWV values are shifted by the corresponding w_c given the temperature
 938 (\hat{q}_{sat} or \hat{T}) time series according to the w_c -temperature relation for WPac [as in (c) and (g)]. The critical
 939 CWV [(c), (g)] and critical CRH [(d), (h)] are calculated for combinations (i) and (ii), respectively. The
 940 colored solid lines in (c) and (g) represent \hat{q}_{sat} conditioned on temperature and CRH ($\equiv \text{CWV} / \hat{q}_{sat}$) $> 60\%$.
 941 This conditional \hat{q}_{sat} is also used in defining the critical CRH. The gray lines in (c) represent CRH from
 942 100% to 80% with 2% spacing.



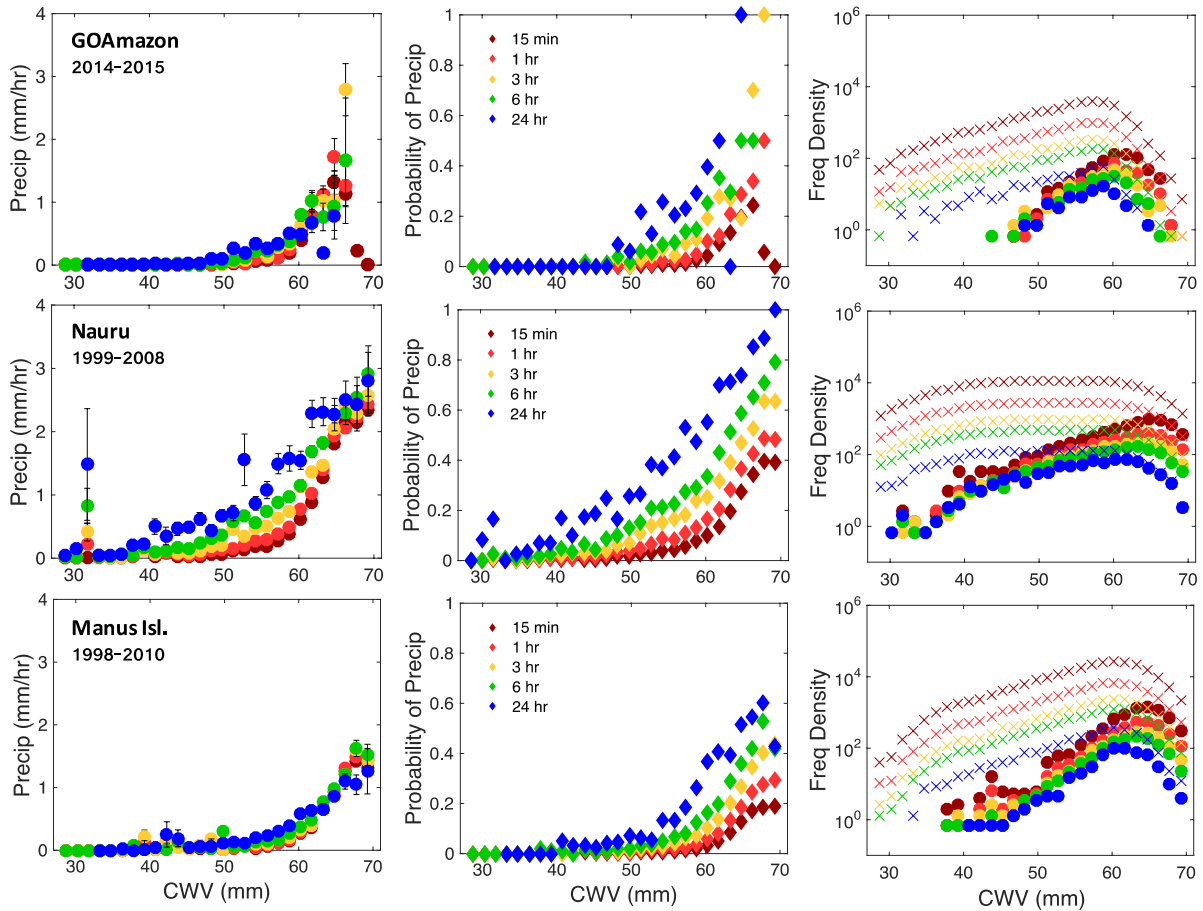
943

944 **Figure 4:** Reanalysis-2 temperature profiles conditionally averaged on TMIv7.1 precipitation and \widehat{q}_{sat} .
 945 Profiles are anomalies with respect to the mean profile averaged over all precipitating events ($P > 0.25$
 946 mm hr^{-1}) with coastal regions excluded.

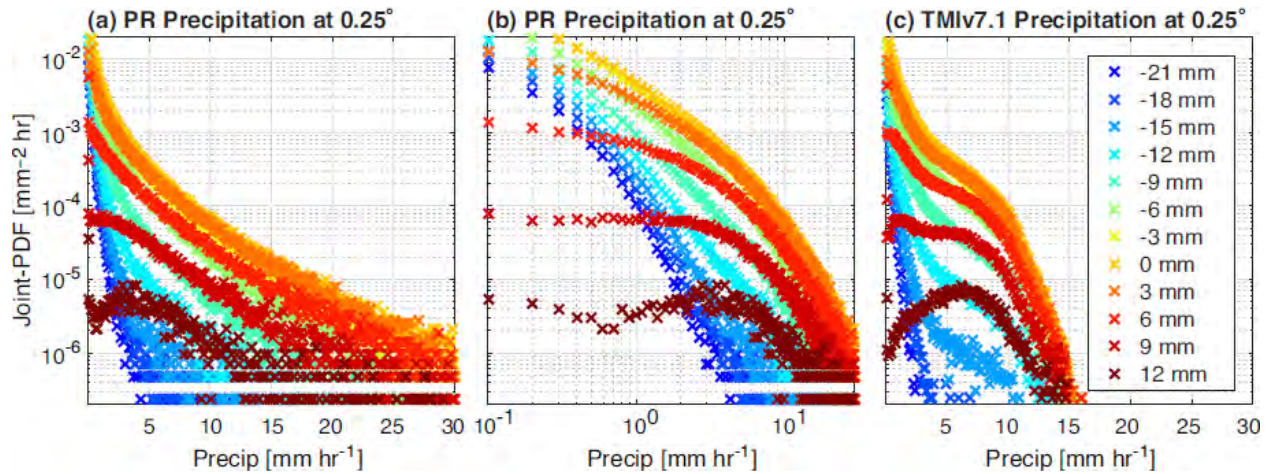


947

948 **Figure 5:** (a) The probability of precipitation as a function of geographical location, calculated using
 949 TMIv7.1 precipitation at 0.25° resolution. (b) The conditional probability of precipitation given CWV
 950 exceeding critical, calculated using TMIv7.1 CWV and precipitation, and Reanalysis-2 temperature at
 951 0.25°. Here the conditional probability is calculated from the frequency binned by $cwv - w_c(\widehat{q}_{sat})$, P ,
 952 and geographical location, with $w_c(\widehat{q}_{sat})$ as in Fig. 3c averaged over four basins. (c) Same as in (b) but at
 953 1°. (d) Same as in (b), but with P defined as the maximum of the TMIv7.1 precipitation rate and two
 954 additional 3B42 precipitation rates that are closest in time to the TMIv7.1 measurement. (e) The fraction
 955 of total precipitation from events with CWV exceeding critical, calculated using data as in (b) at 0.25°. (f)
 956 Precipitation rate (for $P \geq 0.25 \text{ mm hr}^{-1}$) on top of regions of CWV exceeding critical, using TMIv7.1 data
 957 at 1° for ascending orbits on 01 Jan 2004. Note that (f) is a realization of the conditional probability in (c)
 958 on a particular day. For (a)-(e), the precipitation threshold 0.25 mm hr^{-1} is chosen for comparison across
 959 spatial resolution, and CWV offset -1.5 mm to include more events; the magnitudes of
 960 probabilities/fraction in these panels depend on the precipitation threshold and CWV offset, while the
 961 corresponding geographic patterns appear to be robust.



962
 963 **Figure 6:** (Left) Precipitation rate with standard error as error bar, (center) probability of precipitation P
 964 $> 0.5 \text{ mm hr}^{-1}$, and (right) frequency density of all events (crosses) and precipitating events (circles), all
 965 conditioned on CWV using ARM site microwave radiometer CWV and precipitation data for the
 966 GOAmazon site in the Amazon (top), and for Nauru (middle) and Manus (bottom) Islands in the tropical
 967 western Pacific. Here the statistics are calculated using CWV and precipitation data time-averaged at 15-
 968 min (dark red), 1-hr (red), 3-hr (yellow), 6-hr (green), and 24-hr (blue) intervals. Conditional precipitation
 969 without an error bar indicates a standard error smaller than the marker size.

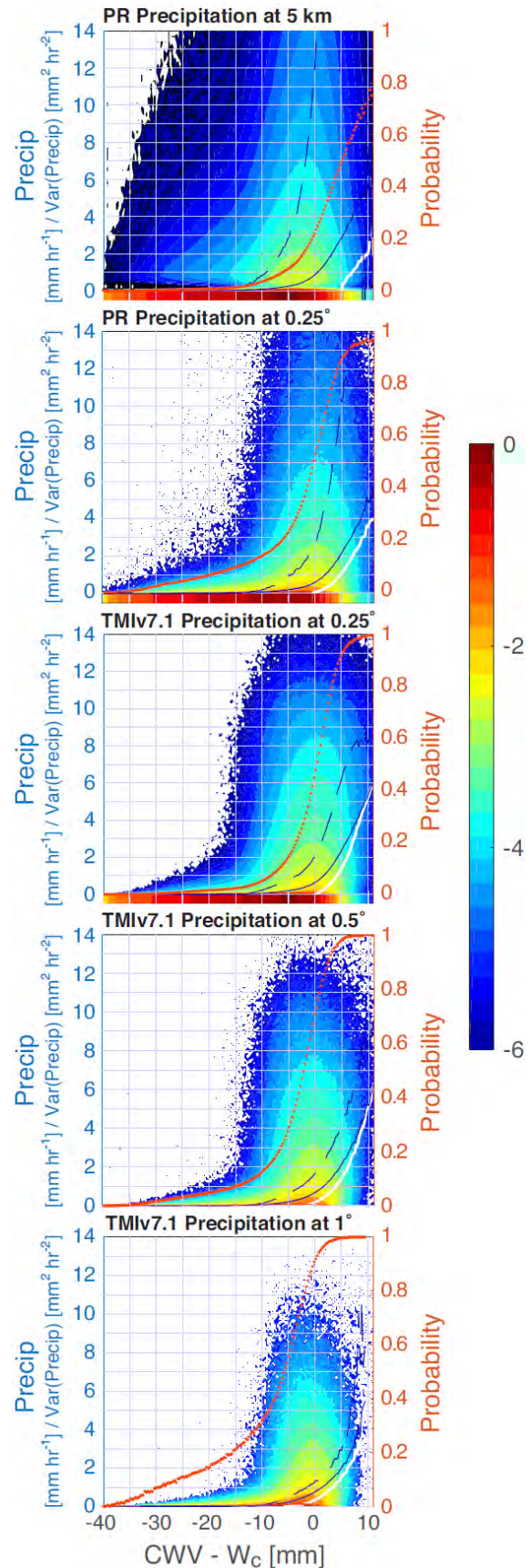


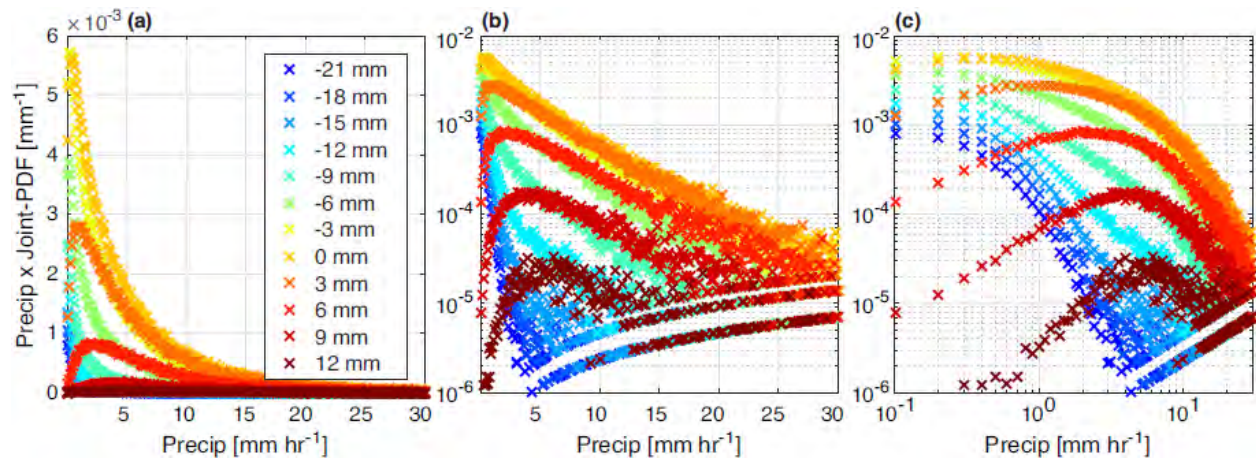
970

971 **Figure 7:** (a) Joint-PDF of CWV relative to critical and precipitation rate P for the 70-mm \hat{q}_{sat} -bin in the
 972 tropical western Pacific compiled using TMIv7.1 CWV, Reanalysis-2 temperature and PR 2A25
 973 precipitation at 0.25° by treating CWV and P as continuous variables with bin-width 3 mm, and 0.1 mm
 974 hr⁻¹ (0.05 for lowest bin), respectively. (b) Same as in (a), but on a log-log scale. (c) Same as in (a), but
 975 using TMIv7.1 precipitation (0.25°). The colors indicate the values of CWV relative to w_c .

976 **Figure 8:** Color shading: Joint-PDF (units: $\text{mm}^{-2} \text{hr}$), on a
 977 \log_{10} -scale, of CWV relative to critical and precipitation
 978 rate P for the 70-mm \widehat{q}_{sat} -bin in the tropical western
 979 Pacific compiled using TMIv7.1 CWV and Reanalysis-2
 980 temperature, PR 2A25 (at 5 km and 0.25°) and TMIv7.1
 981 (at 0.25° , 0.5° , and 1°) precipitation, by treating CWV
 982 and P as continuous variables. The spacing between
 983 the joint-PDF contours is 0.3, i.e., the color advances
 984 whenever the joint-PDF doubles ($10^{0.3} \sim 2$). The
 985 corresponding precipitation rate (blue solid line),
 986 probability of precipitation ($P > 0 \text{ mm hr}^{-1}$; orange
 987 dots), median (white solid line) and variance (blue
 988 dashed line) of precipitation, all conditioned on CWV,
 989 are also shown for reference. For PR (at 5 km and 0.25°)
 990 and TMIv7.1 (0.25°), the bands at the bottom indicate
 991 bins with $0 \leq P < 0.05 \text{ mm hr}^{-1}$. Note that the minimum
 992 nonzero P for raw PR data at 5 km is $\sim 0.11 \text{ mm hr}^{-1}$,
 993 and the TMIv7.1 precipitation at 0.25° is discretized
 994 with units 0.1 mm hr^{-1} .

995





996

997

Figure 9: Precipitation rate-weighted Joint-PDF of CWV relative to critical and precipitation rate P , i.e., the precipitation contribution as a function of CWV and P , for the 70-mm \hat{q}_{sat} -bin in the tropical

998

western Pacific. (a) linear axes; (b) log-linear axes; (c) log-log axes. The data correspond to the Joint-PDF

999

of CWV relative to critical and P in Fig. 7a, using PR 2A25 precipitation at 0.25°. The colors indicate the

1000

values of CWV relative to w_c .

1001